Spatio-temporal dynamics of the Río de la Plata turbidity front; combining remote sensing with in-situ measurements and numerical modeling

Fernanda P. Maciel *[a], Pablo E. Santoro[a], and Francisco Pedocchi[a]

[a] *Instituto de Mecánica de los Fluidos e Ingeniería Ambiental (IMFIA), Facultad de Ingeniería, Universidad de la República. Julio Herrera y Reissig 565, Montevideo, Uruguay, 11300*

fmaciel@fing.edu.uy, psantoro@fing.edu.uy, kiko@fing.edu.uy

November 12, 2020

Abstract

The Río de la Plata is a micro-tidal estuary located in Southeast South America. With an annual mean flow of 26,500 m^3/s, it receives 160 million tons/yr of suspended sediments. The high content of cohesive fine sediments in the estuary generates high turbidity levels in its inner and intermediate zones, which can be clearly seen in color satellite images. In this work, an image-based algorithm was successfully implemented to remotely detect the turbidity front of the Río de la Plata, based on the top of the atmosphere (TOA) reflectance in the red band of MODIS-Aqua satellite. The algorithm finds the reflectance level that 'best' separates two water classes: turbid fluvial and clear ocean waters. The front dynamic was studied combining remotely sensed information and data of river discharge, winds, salinity and sea level time

*corresponding author

series, in the four-year period 2014-2017. River discharge was identified as the main external forcing, revealing a solid general pattern of behavior: when discharge was high (low) the front tended to be located in the outer (intermediate) zone of the estuary. Sea level seemed to be a secondary forcing, presenting higher correlations along the center of the estuary than near both coasts. Local winds needed to have a relatively persistent (2-day) component in a given direction to affect the location of the front. Additionally, results of an already implemented numerical model of the Río de la Plata were evaluated in terms of spatio-temporal performance considering turbidity and salinity fronts locations. New strengths and limitations of the model were identified, and an improvement in the parameterization of sediments' settling velocity was tested. Model results revealed the relative importance of bottom shear stress on the general location of the front, and of salinity on the flocculation process of cohesive sediments. This work provided new insights for the understanding of the Río de la Plata estuarine dynamics through the combination of three complementary tools -remote sensing, in situ data, and numerical modeling-, which may be extended to other systems around the world.

Keywords: satellite images, MODIS, estuary, suspended sediments, salinity, discharge, wind, sea surface level, hydro-sedimentological model

1 Introduction

1.1 The Río de la Plata

The Río de la Plata is a micro-tidal estuary located between Argentina and Uruguay, draining the second largest flow in South America. It is approximately 280 km long and its width increases from 20 km at its inner part to 220 km at its mouth, covering an area of 35,000 km^2. It has both fluvial and estuarine characteristics, and it is usually divided in three zones for its study: inner, intermediate, and outer zone (Figure 1). The intermediate and outer zones can be separated by a transverse limit that extends from Montevideo to Punta Piedras, along which the topographic feature named Barra del Indio is located. Seawards from Barra del Indio a change in bathymetry can be observed, where the water depth suddenly increases, and the salinity front is typically located (Sepúlveda et al., 2004).

The main tributaries of the Río de la Plata are the Paraná and Uruguay rivers, from which it receives a mean annual inflow of 26,500 m^3/s of water and 160 million tons/yr of suspended sediments (Fossati, Cayocca, & Piedra-Cueva, 2014). The suspended sediment load is mainly

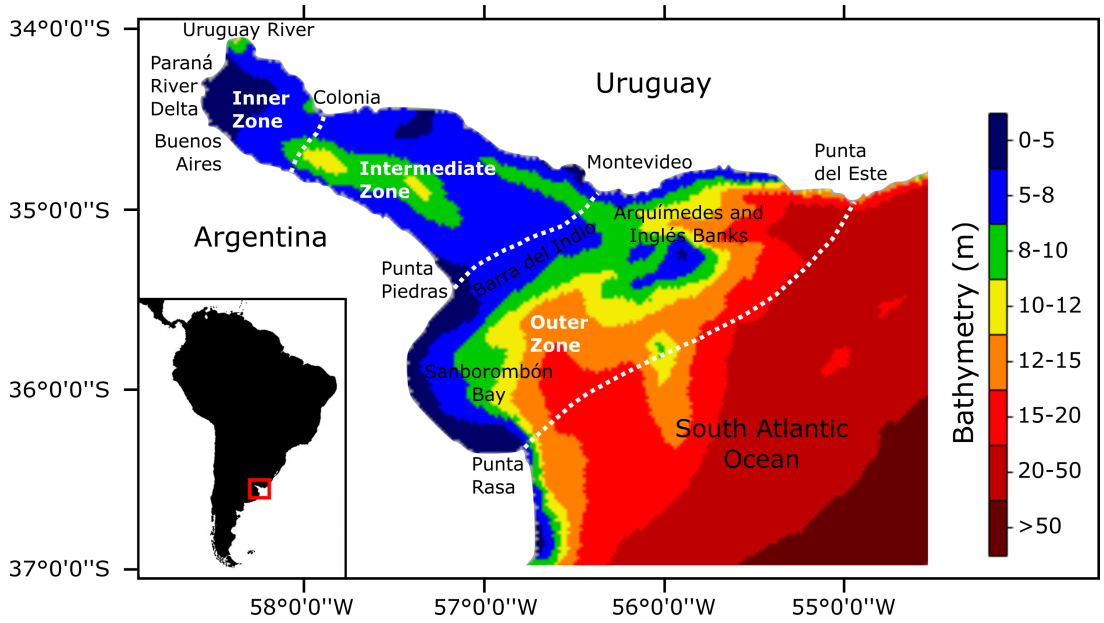

Figure 1: *The Río de la Plata estuary, located between Uruguay and Argentina. Its bathymetry and some characteristic features are indicated.*

the contribution of the Paraná river and it is composed of fine sand, silt, and clay. The sand fraction mostly settles close to the Paraná mouth, while the cohesive sediments are advected into the inner zone of the estuary. The material discharged by the tributaries can take several years to reach the front region, subjected to successive cycles of deposition-resuspension-advection (Fossati, 2013). The highest fine suspended sediment concentration is found near Punta Piedras on the Argentinian coast (Fossati, Santoro, et al., 2014). Towards the Uruguayan coast, the clay content increases along Barra del Indio (Simionato et al., 2011). Regarding bottom material, there is a gradual increase of clay content between the inner and outer zones, with higher values in the northern coast (Moreira et al., 2016). Although the front region is typically located near Barra del Indio, in the course of a year its location can vary hundreds of km along the estuary.

The study and understanding of sediment dynamics in the Río de la Plata, and particularly in the front zone, is of great economic and environmental importance. The Port of Montevideo is located in the front zone of the estuary, and the costs associated with the maintenance of navigation channels and of other coastal engineering works are strongly affected by sediment dynamics in this region. On the other hand, sediments play a relevant environmental role, several substances and contaminants are transported adsorbed to sediments, including pesticides and nutrients (Castro & Reckendorf, 1995; Burone et al., 2006). The concentration of suspended sediments may also affect the penetration of light in the watter column, affecting phytoplankton productivity and the occurrence of potentially harmful blooms (Gobbelaar, 1985; Underwood

& Kromkamp, 1999). Additionally, the spawning of relevant fish species in the Río de la Plata, such as croaker (*Micropogonias furnieri*) and menhaden (*Brevoortia aurea*), is closely linked to the transition between the fresh- and sea-water environments (Berasategui et al., 2004; Acha et al., 2008).

1.2 Remote sensing

Satellite images are able to provide a synoptic view of the estuary and have proved to be useful tools to study its turbidity, which can be related to suspended sediments concentrations. Among previous studies in the Río de la Plata we highlight the pioneering work of Framiñan & Brown (1996). They used 4 years of AVHRR satellite images, from 1986 to 1990, to qualitatively study the temporal and spatial distribution of the turbidity front. Nagy et al. (2008) studied the relationship between river flow and winds with the maritime and turbidity fronts. They worked with SeaWIFS imagery for the period 2000-2003, including both El Niño and La Niña events. Piola et al. (2008) used information from the SeaWIFS satellite as well, but focused on the study of the plume influence over the Southwestern South Atlantic continental shelf.

Regarding quantitative estimations of sediment concentrations in the Río de la Plata, we should highlight the works of Moreira et al. (2013) and Dogliotti et al. (2016). The former used the algorithm proposed by Gohin (2011) applied to 10 years of MODerate resolution Imaging Spectroradiometer aboard the Aqua satellite (MODIS-Aqua) images to analyze the mean distribution and seasonal cycles of the material in suspension in the Río de la Plata; whereas the latter used 15 years of MODIS sensors images to study the seasonal and inter-annual variability of turbidity in the estuary.

In other parts of the globe, MODIS imagery has been used to study spatio-temporal variability of river plumes and suspended sediment concentration in coastal areas. Some recent examples are Petus et al. (2014); Di Polito et al. (2016); Fernández-Nóvoa et al. (2017, 2019); Zhan et al. (2019).

1.3 Main contributions

This work adds to the ones listed above by first proposing an image-based, autonomous algorithm to detect the turbidity front. This information was combined with ground data -river discharge, local winds, and in-situ measured salinity and sea surface level over the Uruguayan coast-, to study their influence on the turbidity front location. Statistical correlations were computed to

quantify the link between different variables and the front position, considering temporal lags between them. We applied the developed algorithm to images acquired by the MODIS-Aqua satellite over the Río de la Plata, from 2014 to 2017, which were selected due to the availability of in-situ data.

A second contribution of this work is the novel use of turbidity fronts detected from satellite information to evaluate the performance of a previously developed hydro-sedimentological model of the Río de la Plata (Santoro, 2017). This approach allowed us to gain a better understanding of the model's strengths and limitations, and to identify potential improvements. One of them, the effect of salinity on the flocculation of cohesive sediments, was explored in this work. Model results and analyses from previous works were considered to enrich the discussion and to better understand the studied processes.

2 Data and methods

2.1 Remote sensing

2.1.1 Previous approaches

In the Río de la Plata turbidity and salinity fronts are generated when the very turbid, fresh, river water, and the clear, saline, ocean water meet, resulting in large horizontal gradients of turbidity and salinity. From these two variables only near-surface turbidity can be detected by optical sensors due to sharp gradients in emitted radiance. Nagy et al. (2008) defined frontal boundaries as sharp changes in water color in SeaWIFS images. Similarly, Framiñan & Brown (1996) related the front with a strong gradient in reflectance and sharp change in water color in the visible and near infrared (NIR) channels of AVHRR sensor. They also related the front with the estuarine turbidity maximum, a zone of highest turbidity resulting from turbulent resuspension of sediments. Both authors digitized the front manually, taking into account the distribution of maximum reflectance and the most seaward position of the maximum gradient of reflectance values.

2.1.2 Satellite data

In this study we used the red channel (wavelength of 645 nm) reflectance to detect the turbidity front in MODIS-Aqua images. Turbidity has been directly related to reflectance in the red band of the visible light spectrum (Dogliotti et al., 2015). Additionally, the shortwave infrared band

(SWIR, 1240 nm) was used for the land mask, while the red (645 nm) and NIR (856 nm) bands were used for cloud detection. The area delimited by the following coordinates was considered: 54.7° to 58.7° W and 33.8° to 37.3° S. The land was masked following a similar procedure as the one described below for detecting the front: based on the image histogram but for the SWIR band. Clouds were masked following thresholds recommended by Ackerman et al. (2006), slightly adapted for the region; specifically: when reflectance at the red band was higher than 0.22, or when it was higher than 0.18 and the NIR/red ratio was between 0.9 and 1.1. If a pixel was identified as a cloud, neighbor pixels were also masked. An image was discarded if 40% of the considered subset is covered by clouds, or if more than 80% of the water pixels were masked. Approximately 100 images per year were kept, as shown in Table 1. We used top of the atmosphere (TOA) reflectances (level 1B data) obtained from the Atmosphere Archive & Distribution System (LAADS), which contained calibrated and geolocated at-aperture radiances. The images had a spatial resolution of approximately 1 km and were available with a daily time step. An atmospheric correction was not applied; which would be important if we were trying to estimate quantitative water properties (Dogliotti et al., 2016). However, in this work only relative differences in reflectance over the image are considered (Figure 2(a)).

Table 1: *Number of available MODIS-Aqua images per month and per year (after cloud discard).*

	Jan	Feb	Mar	Apr	May	Jun	Jul	Aug	Sep	Oct	Nov	Dec	**Tot**
2014	12	1	9	7	6	8	9	12	9	10	15	15	113
2015	13	11	14	13	7	9	7	4	12	1	9	13	113
2016	10	16	7	3	0	2	5	8	3	7	13	16	90
2017	14	8	11	8	7	5	6	7	8	4	13	12	103
Tot	49	36	41	31	20	24	27	31	32	22	50	56	419

2.1.3 Detection of the turbidity front

A continuous turbidity maximum was not always observed across the estuary, as the maximum gradient many times presented discontinuities in the satellite images, posing difficulties in the development of an algorithm to detect a continuous front. However, as it can be observed in Figure 2(a), there is a clear distinction between the high reflectance of turbid river water and the negligible reflectance of clear seawater. Hence, the turbidity front was defined as the reflectance level that 'best' separated these two waters, using the method of Otsu (1979) to segment the image. It is an optimum global thresholding method, based on the histogram of the image (Figure 2(b)). The two classes (turbid and ocean waters) are clearly distinct with respect to

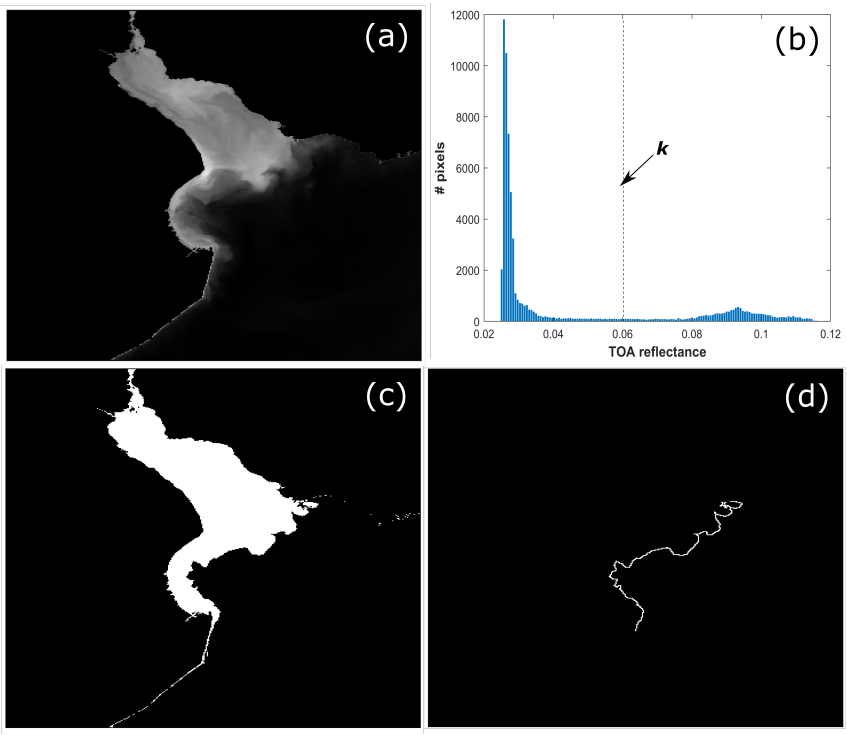

Figure 2: *Upper panels show an example of TOA reflectance in the 645 nm channel of MODIS-Aqua satellite (a) and its histogram (b) for December 25th, 2015. Reflectance level k in panel (b) is identified using Otsu's method. Lower panels show the application of Otsu's method to segment the image into two regions (c) and detection of the turbidity front as the border between them (d).*

their pixels' intensity values (i.e., reflectance), and an optimum is found that maximizes the between-class variance, defined as:

$$\sigma_B^2(k) = P_1(k)\,(m_1(k) - m_G)^2 + P_2(k)\,(m_2(k) - m_G)^2\,, \qquad [1]$$

where k is the threshold level, $P_1(k)$ and $P_2(k)$ are the probabilities that a pixel is assigned to class 1 or 2 respectively, $m_1(k)$ and $m_2(k)$ are the mean intensity values of pixels assigned to classes 1 and 2 respectively, and m_G is the average intensity of the entire image (i.e., the global mean). The between-class variance is a measure of separability, since the farther the two means m_1 and m_2 are from each other, the larger $\sigma_B^2(k)$ will be. Given a value of k, P_1 was computed as the number of pixels that had an intensity level smaller than k divided by the total number of pixels in the image, and $P_2 = 1 - P_1$. Equation [1] was evaluated for different threshold levels and the one that gives the largest $\sigma_B^2(k)$ was selected. The range of intensities in each image was divided into 200 discrete intervals, and only water pixels were considered. Figure 2(c) shows an example of segmentation into two different classes. The segmented image

was smoothed with a median filter of 3×3 pixels and the boundary was found by subtracting the smoothed and original segmented images. To obtain a continuous front, a numerical tag was assigned to all pixels detected as boundaries. Pixels that were connected to each other (8 neighbors connectivity: 4 sides and 4 corners) were assigned the same tag number, while it changed for disconnected pixels. Finally, pixels that were flagged with the most repeated tag were kept (i.e., the continuous boundary with the largest number of pixels, Figure 2(d)). Note that the threshold level k could vary among different images. This is important, firstly, because images were not corrected for atmospheric conditions; and secondly, because the turbidity front represents the transition between river water with higher concentrations of suspended sediments and clear ocean water, and the turbidity of river water may vary along the year.

The distribution of the front location was analyzed over the period 2014-2017. In each image, pixels where the front was located were given a value of 1, and 0 otherwise. A Gaussian filter was then applied to the image in order to smooth the position of the detected front, and then the image was re-normalized so that the maximum value was 1. Finally, the images were averaged to obtain the occurrence frequency of the front at each location (Figure 3).

In order to study the temporal evolution of the turbidity front, and compare it to other variables, its distance along the estuary in the SE-NW direction was computed along three lines: one near the N coast, one along the center of the estuary, and one closer to the S coast (Figure 3). Distances along these lines are referred to the mode of the front location on each of them, being positive to the SE and negative to the NW.

2.2 In-situ variables

Daily discharges of the main tributaries, the Paraná and Uruguay rivers, are available between January 1980 and March 2018 from the Instituto Nacional del Agua (INA, `www.ina.gov.ar`), Argentina. The mean flow rates over the whole record are 20,090 m^3/s for the Paraná river, 6,470 m^3/s for the Uruguay river, and 26,560 m^3/s for their combined discharge. The mean discharge for the period considered in this work (2014-2017) was 21,060 m^3/s for the Paraná river, 8,700 m^3/s for the Uruguay river, and 29,760 m^3/s for their combined discharge.

Wind data were obtained from the European Centre for Medium-Range Weather Forecasts (ECMWF). The ERA-Interim reanalysis (Dee et al., 2011) was used, which has a six-hour time step and spatial resolution of 0.125°. Points across the width of the estuary were selected, along Barra del Indio (Figure 3): one approximately 30 km off the coast of Montevideo (latitude 35.1°

S, longitude 56.4° W), one in the central part of the estuary (latitude 35.3° S, longitude 56.4° W), and another one closer to the southern coast (latitude 35.5° S, longitude 56.7° W).

In-situ salinity was measured with SBE 19 plus CTDs in two sites along the northern coast of the Río de la Plata (Figure 3): at Gas Sayago (GS), located near Montevideo Bay (latitude 34.930° S, longitude 56.274° W); and at Punta del Tigre (PT), approximately 40 km W from Montevideo (latitude 34.763° S, longitude 56.538° W). Both time series had a time step of 1/2 hour; the former was available only for the year 2015, while the latter covered from December 2014 to December 2017. In GS the mean water depth was 7 m, and the salinity measurements were taken 0.7 m below the water surface, while in PT the mean water depth was 4 m, and the salinity measurements were taken 0.5 m above the bed.

Hourly sea surface level data were available at Montevideo Bay (N coast, Figure 3) from September 2014 to October 2017. For the present study, and after a detailed analysis, a moving average of seven days was applied to the data. This processing removed the astronomical components of the tide, as the frequency of available (cloudless) MODIS images was not adequate to study the direct effect of astronomical tides on the location of the turbidity front. Nevertheless, their indirect influence through bottom shear stress is Discussed in Section 4.1. The averaged sea level better represents meteorological tide events that lasted for several days, mainly associated to winds in the continental shelf, as it is discussed in Section 4.3.2.

2.3 Numerical model

2.3.1 Description of the model

The 3D hydro-sedimentological model used in this work had been previously implemented for the Río de la Plata estuary by Santoro (2017). It was implemented on the open-source TELEMAC-MASCARET suite of solvers (EDF - LNHE, 2020). The module TELEMAC3D applies finite element solution methods to solve the Navier–Stokes equations for free surface flows and advection-diffusion equations for the transport of passive or active substances like salt or suspended solids (Hervouet, 2007). The equations are solved on an unstructured grid of triangles in the horizontal with a sigma transformation used to project the horizontal triangle cell into a series of prisms dividing up the vertical. The various variables in the equations (bed elevation, free surface level and velocity components) are defined at the nodes (vertices of triangles). Wave generation and propagation are simulated using the third generation spectral wave model TOMAWAC. It solves the conservation equation of wave action density within a directional

spectrum, including processes like wind-driven wave generation, energy dissipation by white capping, bottom friction, and wave breaking as well as wave transformation due to shoaling, and wave–wave interaction.

The simulated domain included the entire Río de la Plata estuary and the Atlantic continental shelf. The grid resolution varied from 12 km at the ocean boundary to 10 m inside Montevideo Bay, which was the original focus of the model. On the vertical direction 15 equally distributed sigma layers were used. The model takes as boundary conditions: discharges of the Paraná and Uruguay rivers (daily mean flow rates and constant mean suspended sediment concentrations); tides (astronomical and meteorological) and waves at the oceanic boundary from regional models (Martínez et al., 2015; Alonso et al., 2015); and wind and sea level pressure from the ECMWF ERA-Interim Reanalysis (Dee et al., 2011). Both the salinity and suspended fine sediments are considered in the simulations and modify the fluid density.

The model implementation was focused on the fine cohesive sediments dynamics, non-cohesive sediments were not considered. TELEMAC3D is able to solve the coupled hydrodynamic, bed evolution and suspended sediment transport of uniform sediments (cohesive or non-cohesive). For cohesive sediments the bed evolution is computed using a mass balance equation in which the erosion and deposition fluxes are computed using the classical Krone and Partheniades laws. The critical shear stress for erosion and deposition were set at 0.1 N/m^2 and $1x10^4$ N/m^2 (simultaneous erosion-deposition paradigm). The erosion rate in the Partheniades equation was set at $3x10^{-4} kg/m^2 s$. As only fine sediment were considered, areas where non-cohesive sediments are predominant were set as non-erodables. The model solves the suspended sediment transport using an advection-diffusion equation including an additional term to represent the sediment vertical settling (Benson et al., 2014). Details on the settling velocity parametrization are given in the Section 2.3.2.

The simulation results had an hourly temporal resolution and covered the year 2015. The model was calibrated and validated with in situ data (sea surface level, currents, suspended sediment concentration or turbidity and salinity) from point time series located in different zones of the estuary and particularly near Montevideo Bay over extended periods of time. It presented an excellent performance in the prediction of surface water levels , which in the Río de la Plata are strongly conditioned by meteorological conditions; and a good performance in the prediction of turbidity (suspended sediment concentration) and salinity in locations close to Montevideo where data was available (Santoro, 2017; Santoro et al., 2016). Besides its calibration

240 and validation with point time series, the model had never been validated in terms of the overall
241 front dynamics.

242 2.3.2 Settling velocity parameterization

The sediments of the Río de la Plata, particularly close to Montevideo are dominated by silt and clay (Fossati, Santoro, et al., 2014). These sediments are able to flocculate changing their average settling velocity. In the original implementation of the numerical model, flocculation of fine sediments was included with a variable settling velocity (ω_s), function of the suspended sediment concentration (C) only,

$$\omega_s = \omega_{s0} \times g(C), \quad [2]$$

where w_{s0} is the reference settling velocity at a concentration $C_0 = 100$ mg/L, equal to 0.3 mm/s, and $g(C)$ is a linear function (van Leussen, 1999),

$$g(C) = C/C_0; \quad [3]$$

243 further details regarding the model calibration parameters can be found in Santoro (2017).

For the purpose of the present work, an additional parameterization was evaluated, which incorporates the effect of salinity (S)

$$\omega_s = \omega_{s0} \times g(C) \times f(S), \quad [4]$$

where w_{s0} is the reference settling velocity (without salinity), and $f(S)$ is a function of the form (Gourgue et al., 2013)

$$f(S) = \begin{cases} 1 & \text{if } S < S_L \\ (P_s - 1) \times \frac{S - S_L}{S_H - S_L} + 1 & \text{if } S_L \leq S \leq S_H \\ P_s & \text{if } S > S_H \end{cases} \quad [5]$$

244 From equation [5] it can be observed that $f(S)$ is linear when S is between S_L and S_H, and
245 otherwise it is constant, considering the fact that an effect on flocculation is neither observed for
246 very low salinities ($< S_L$), nor for very high ones ($> S_H$). The new parametrization incorporated
247 the parameters S_L, S_H, and P_s. S_L and S_H were selected as 1 and 15 psu, respectively, based

on Mehta (2014); Xia et al. (2004). w_{s0} and P_s were left as calibration parameters, the former is the reference settling velocity in fresh water at a C of 100 mg/L, while the latter represents the factor by which w_s is incremented in the presence of saline water (when $S \geq S_H$) for any given C. Several sets of parameters were considered, with w_{s0} between 0.05 and 0.2 mm/s, and P_s ranging from 3 to 6. Finally, w_{s0} was selected as 0.2 mm/s and $P_s = 4$, as it was the combination that resulted in realistic suspended sediments concentrations, preserving the general sediment dynamics behaviour obtained with the original model. Hence, for a C of 100 mg/L the sediments have a lower settling velocity of 0.2 mm/s in the presence of fresh water, while in saline water w_s was increased to 0.8 mm/s. None of the other model parameters were modified. A more thorough calibration considering all parameters will be pursued in future works, but it was out of the scope of this study.

2.3.3 Detection of surface turbidity and salinity fronts

The numerical model allowed us to analyze the results of both turbidity and salinity fronts. The algorithm described in Section 2.1.3 was applied to the suspended sediment concentration (SSC) results. The model results were first interpolated to a regular grid of 1×1 km, and the intensity of each pixel was computed averaging the concentration over the top 4 vertical layers, as these were considered to give results comparable to the satellite observations.

On the other hand, the salinity front was defined as the isoline of 10 psu considering the depth-averaged salinity in the water column, which is a reasonable value to select considering the effects of salinity in sediment's flocculation processes. A discussion regarding the interpretation of these fronts is included in Section 4.

3 Results

3.1 Remote sensing

In this Section we study the location of the turbidity fronts obtained from MODIS images, as well as it relationship with in-situ data. This allowed us to identify the main forcing influencing front dynamics.

3.1.1 Overall location

The most frequent position of the front matched approximately the location of Barra del Indio (Figure 3). However, the turbidity front location presented a large variability both over the whole four-year period (2014-2017) and over each individual year. It is noticeable the differences between the behavior of the front over the northern and southern coasts: along the former it is more disperse, while along the latter it usually followed the coast in Sanborombón Bay. These differences in behavior are discussed in Section 4.1, in terms of bathymetry, bottom shear stress and bottom material.

It was observed that during the study period the front reached the Atlantic Ocean boundary a few number of times along the three lines (N coast, Center and S coast), and it reached the furthest inner locations into the estuary along the N coast.

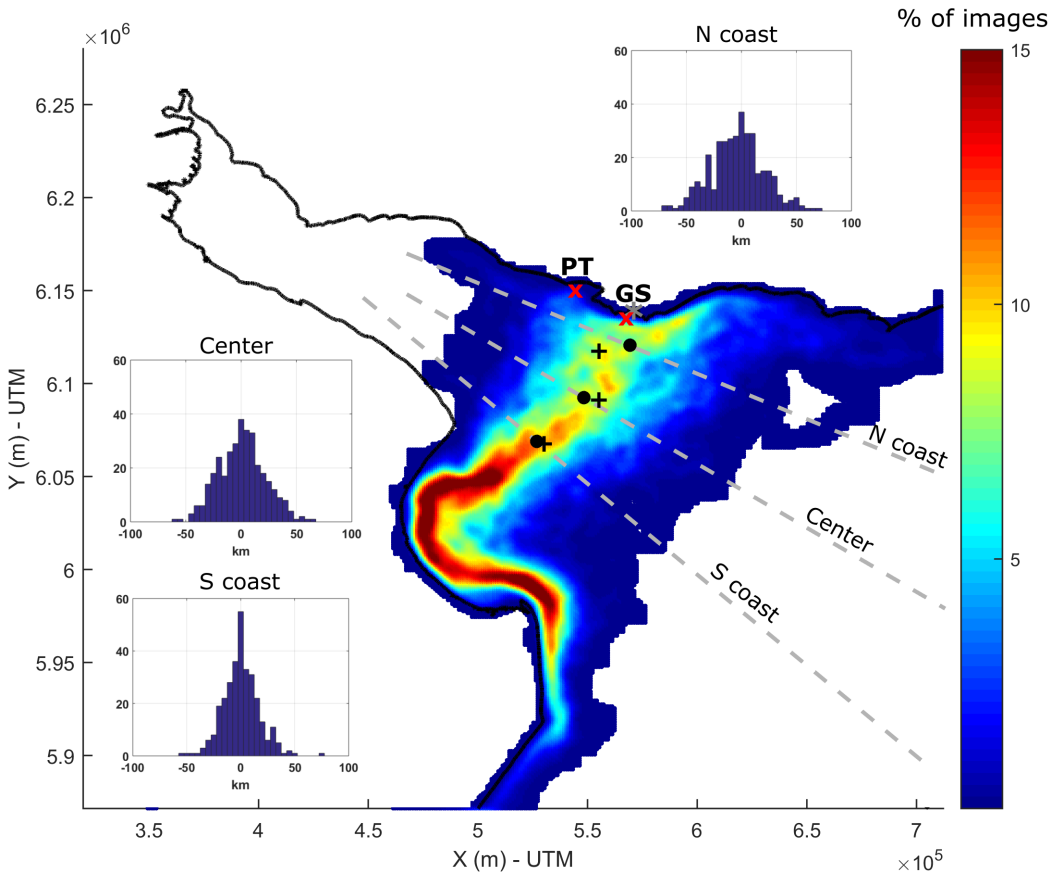

Figure 3: *Location of the turbidity front during 2014-2017, obtained from MODIS-Aqua images. The values represent approximately the percent of images at which the front was detected at a given place. Dark dots indicate the mode (most frequent location) along three dotted lines that are approximately orthogonal to the front average location. + symbols show wind data points, × symbols show salinity continuous measurements at PT and GS, and * symbol indicates Montevideo Bay, where sea level is measured.*

In Figure 3, the histograms of the turbidity front location along each of the previously defined SE-NW lines, are presented with bins of 5 km. Over the N coast line, the front was found to go as far as 70 km away from its mode, both in the SE and NW directions; the distribution was nearly symmetric, with 55% of the images showing the front located to the NW, and 45% to the SE. Over the center line, the front reached locations up to 60 km to the NW and 65 km to the SE. Over the S line, the front reached locations up to 55 km to the NW and 75 km to the SE. Histograms for both the center an S lines were fairly symmetric. However, the histogram for the S line was narrower, with a much more frequent mode.

3.1.2 Temporal evolution

The time series of the turbidity front distance along the N coast is shown using bars in Figure 4, together with continuous lines representing salinity at PT and discharge anomalies. For visualization purposes, the latter were computed relative to the study period's mean discharge. Salinity at PT was generally low, being less than 5 psu 90% of the time, but reaching up to 25 psu in small number of occasions. Higher salinity values were not sustained for long periods of time and they were always associated to sharp peaks in the scale of hours and days.

Figure 4 shows a general relation between discharge, salinity and the position of the turbidity front along the N coast. When salinity was high at PT, the front was retreated towards the inner part of the estuary, and this typically matched negative anomalies of total discharge, for example, from February to July of 2015, and December 2016 to February 2017. On the other hand, when positive anomalies of river discharge occurred, the front tended to be located towards the outer zone of the estuary, for example, from July to September of 2014, and December 2015 to July 2016.

The time series of smoothed sea level at Montevideo Bay is also included in Figure 4. The relationship between sea level and the turbidity front distance along the N coast was visually less robust. However, in general, it could be observed that salinity peaks recorded at PT were associated with rising sea levels, after a strong negative anomaly.

3.1.3 Relation to river discharge

The relation between river discharge and the location of the turbidity front can be further observed in Figure 5. Along the N coast, when total discharge (Q RdlP) was higher (lower) than 30,000 m^3/s, the front tended to be located to the SE (NW) of its mode. Visually analyzing the

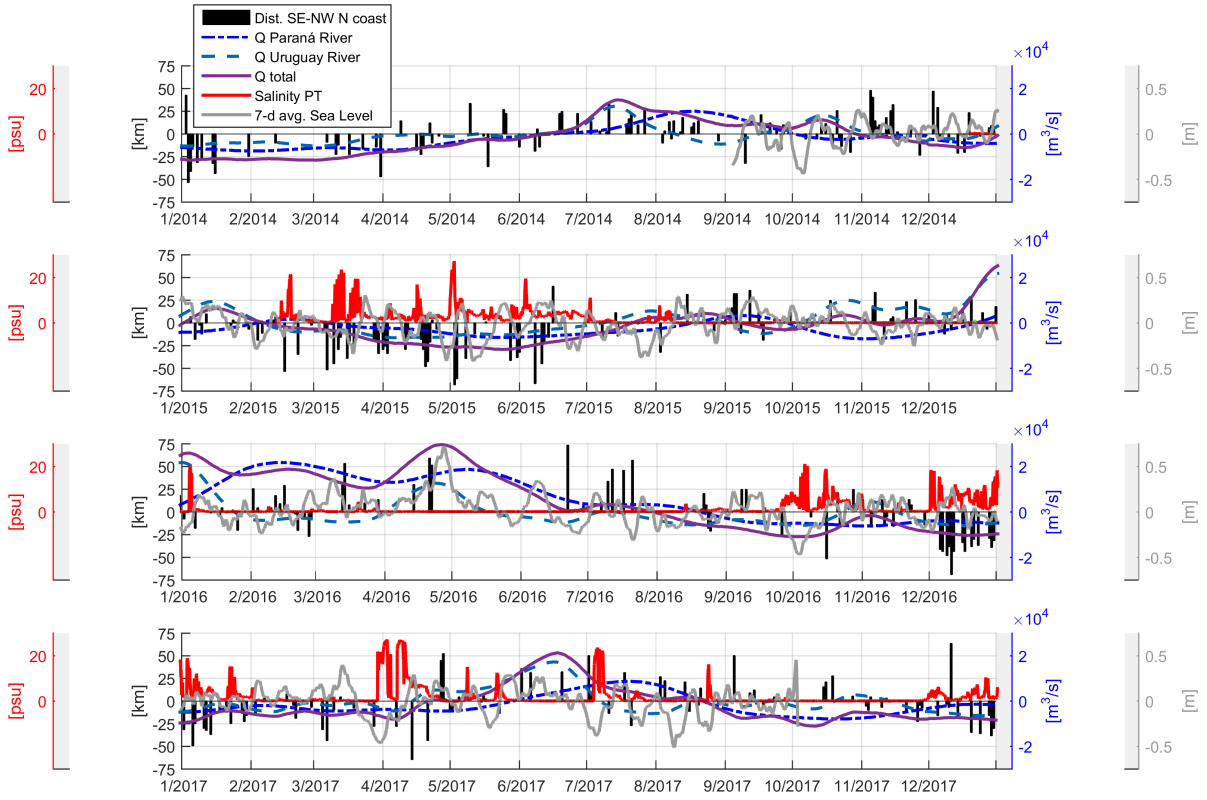

Figure 4: *Time series of turbidity front distance (in km, relative to its mode) along the N coast in the SE-NW direction. Discharge (Q) anomalies (in m^3/s), salinity (in psu) at Punta del Tigre (PT), and anomalies of smoothed sea level in Montevideo Bay (in m with a moving average of 7 days) are also included.*

role of the main tributaries in this figure, individually and combined, the role of the Uruguay river seemed to be the most important. However, quantitative results presented in Table 2 showed that the highest correlation was actually obtained when the combined river discharge was considered.

From Figure 5 it can also be observed that the highest variability corresponded to the lower discharges. Another interesting observation is that the relationship between discharge and the front location decreases towards the southern coast of the estuary. To further explore these observations, Figure 6 shows the distribution of the front location for the upper (Figure 6(a)) and lower (Figure 6(b)) discharge quartiles during 2014-2017. It is clear that, along the S coast, the front location is essentially the same in both panels. However, along the N coast, the front shifts towards the outer (intermediate) zone as discharge increases (decreases).

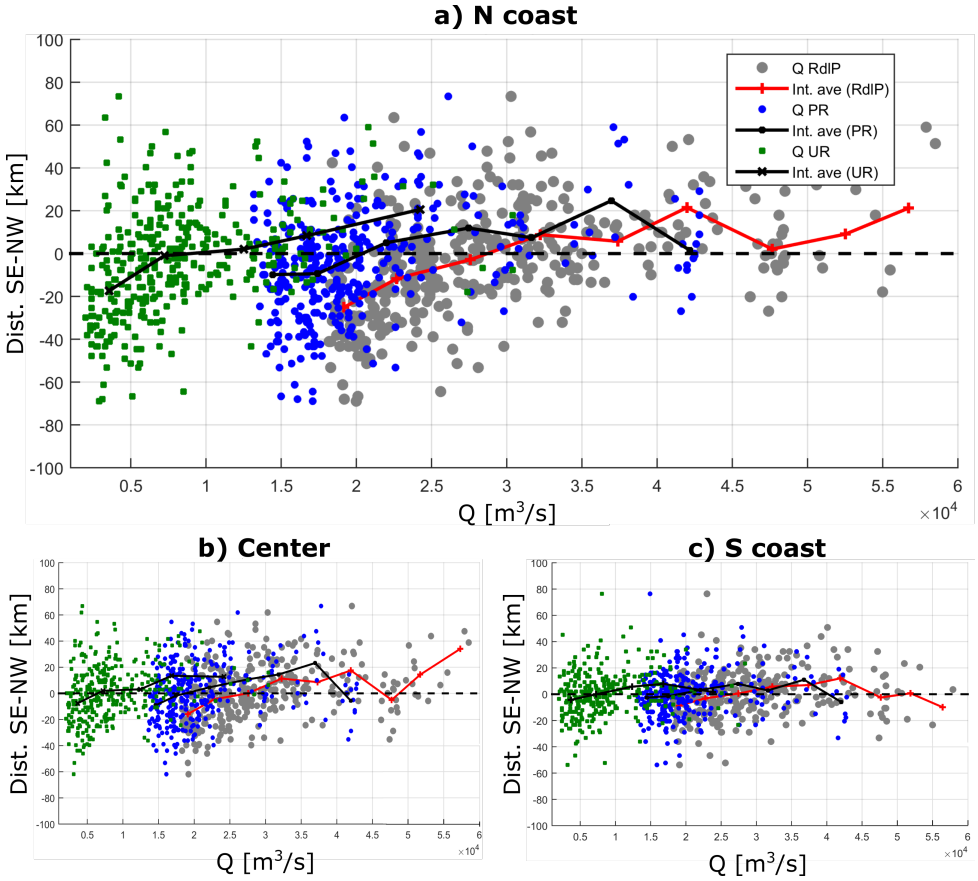

Figure 5: *Distance of the turbidity front (in km, relative to its mode) in the SE-NW direction along the N coast (a), the center (b), and the S coast (c) of the estuary versus river discharge (RdlP: Río de la Plata; PR: Paraná river; UR: Uruguay river). Interval averages are included to indicate the general trend.*

Table 2: *Pearson (Spearman) correlations between SE-NW distance of the turbidity front relative to its mode and river discharge (RdlP: Río de la Plata; PR: Paraná river; UR: Uruguay river). Bold values indicate p-values lower than 0.05.*

		2014	2015	2016	2017	2014-2017
N coast	RdlP	**0.42(0.45)**	**0.52(0.60)**	**0.41(0.49)**	**0.42(0.34)**	**0.43(0.51)**
	PR	**0.35(0.43)**	0.17(0.12)	**0.35(0.32)**	0.21(0.02)	**0.28(0.31)**
	UR	**0.33(0.37)**	**0.49(0.59)**	**0.27(0.42)**	**0.39(0.40)**	**0.36(0.44)**
Center	RdlP	**0.41(0.43)**	**0.53(0.65)**	**0.25(0.24)**	0.17(0.10)	**0.33(0.39)**
	PR	**0.35(0.43)**	**0.24**(0.19)	0.17(0.16)	0.10(0.09)	**0.21(0.26)**
	UR	**0.30(0.27)**	**0.48(0.60)**	**0.25**(0.19)	0.14(0.10)	**0.29(0.34)**
S coast	RdlP	**0.34(0.34)**	**0.46(0.48)**	-0.003(0.02)	0.16(0.09)	**0.20(0.28)**
	PR	**0.24(0.31)**	0.16(0.10)	0.02(-0.005)	**0.24**(0.22)	**0.12(0.18)**
	UR	**0.33(0.36)**	**0.41(0.48)**	-0.05(-0.01)	0.02(-0.01)	**0.18(0.22)**

3.1.4 Relation to local wind

The wind roses (across the width of the Río de la Plata) for the study period showed that the most frequent winds came from de N-E quadrant and had in general magnitudes lower than 10

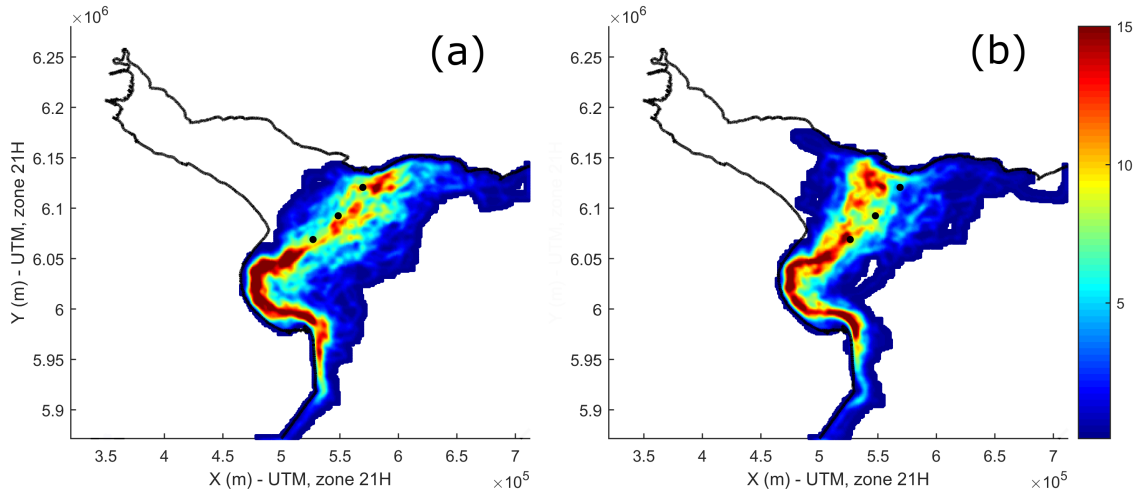

Figure 6: *Location of the turbidity front segregated according to quartiles of total daily river discharge. Panel (a) shows cases with discharges higher than its 75th percentile, and panel (b) cases with river discharge lower than its 25th percentile. Discharges associated with these percentiles are 33,600 m^3/s and 22,500 m^3/s, respectively. The colors represent the percent of images at which the front was detected at a given place. The number of images included in each panel was 81 for (a) and 93 for (b); dark dots indicate the mode considering all images along the three lines defined in Figure 3.*

m/s. However, the strongest winds, reaching over 20 m/s, came from the S-W quadrant. No relationship was found between the location of the turbidity front and the instantaneous wind closest to the satellite's acquisition hour.

Considering that the effect of the wind on the global position of the front might no be instantaneous, and after a detailed analysis, the average of the wind vector over a two-day window prior to MODIS acquisition time was used in the analysis. We found that the majority of the detected fronts were associated with winds below the 50th percentile. This suggests that stronger winds are associated to an increase on the presence of clouds, when images are more often discarded.

In order to better analyze the possible influence of persistent winds, Figure 7 shows the distribution of the turbidity front location for two-day averaged winds exceeding 5 m/s during the period 2014-2017. Each panel shows the front distribution for winds coming from each of the four quadrants. Some differences can be clearly appreciated: for N-W winds, the front remained close to its most frequent location, but slightly inwards (Figure 7(a)); for N-E winds, the front tended to be towards the outer zone of the estuary along the center and S coast, and more often inwards along the N coast (Figure 7(b)); for S-W winds, the turbidity front was most often found in the outer zone of the Río de la Plata along the N coast (Figure 7(c)), with one exception observed during a very low river discharge event; finally, for S-E winds, the front location was

close to its most frequent location (Figure 7(d)). Additionally, we computed correlations of the turbidity front distance along each line (defined in Figure 3) with wind projections in the NW-SE direction (along the estuary axis) and in the NE-SW direction (perpendicular to the estuary axis), but the obtained coefficients were relatively low and not statistically significant.

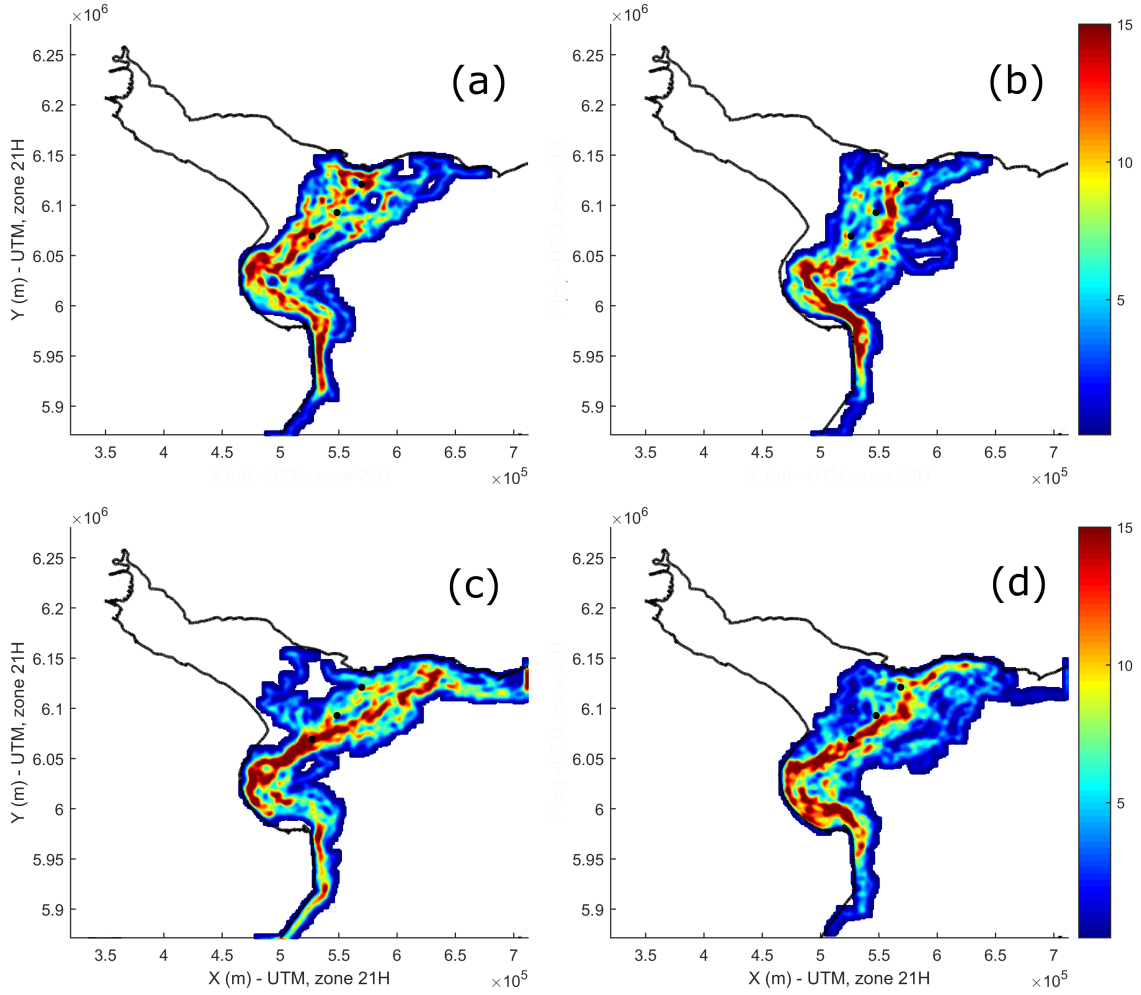

Figure 7: *Location of the turbidity front for (two-day averaged) winds from different quadrants: N-W (a), N-E (b), S-W (c), and S-E (d). In all cases the average wind magnitude is larger than 5 m/s, and for panel (c) it is larger than 6 m/s. The colors represent the percent of images at which the front was detected at a given place. For each panel the number of images is approximately the same (20); dark dots indicate the mode considering all images along the three lines defined in Figure 3.*

3.1.5 Relation to sea level

It was found that a seven-day window with a lag of four days produced the highest correlations between sea level in Montevideo Bay and salinity at PT, as it is presented in Table 3. As shown in this table, the line along the S coast presented the lowest correlation, which may be expected as it is the farthest one from Montevideo Bay, where sea level was measured. However, the

highest correlation was obtained for the line located at the center of the estuary, and not for the N coast line, which is the one closest to the Bay.

Figure 8 shows the position of the front for upper and lower seven-day averaged sea level quartiles with a lag of four days. When the sea level was high in Montevideo Bay (Figure 8(a)), a few days later the front tended to be located to the SE along the center of the estuary; while closer to the N coast it had two preferred locations. On the other hand, when the level was low (Figure 8(b)), the front tended to be a few days later in the intermediate zone along the center, reaching further inner locations along the N coast.

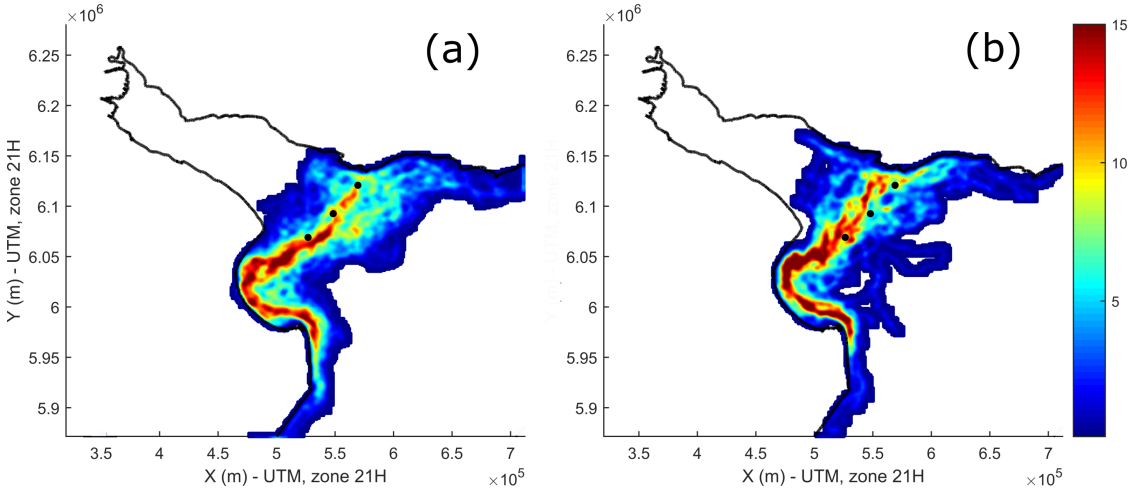

Figure 8: *Location of the turbidity front segregated according to quartiles of 7-day averaged sea level in Montevideo Bay with a lag of 4 days. Panel (a) shows cases with average sea level higher than its 75th percentile 4 days prior to the satellite's acquisition date, and panel (b) cases with average sea lever lower than its 25th percentile 4 days prior to the satellite's acquisition date. Sea level values associated with these percentiles are 1.18 m and 0.99 m, respectively. The colors represent the percent of images at which the front was detected at a given place. The number of images included in each panel was 75 for (a) and 48 for (b). Dark dots indicate the mode considering all images along the three lines defined in Figure 3.*

3.1.6 Relation to in-situ salinity

The PT field station is located very close to the N coast line defined in Figure 3, and approximately 40 km NW of the turbidity front's mode. Its salinity measurements seemed to define a threshold for the location of the front, as shown in Figure 9. When salinity at PT was greater (lower) than 2 psu, the front was almost always found to the NW (SE) of its mode. Regarding the few exceptions to this general trend that can be observed in Figure 9, the case with relatively high salinity (17.4 psu) and SE location of the front coincided with high river discharge (larger than the 75th percentile); and the two exceptions with salinity closer to 5 psu (3.6 and 4.5 psu)

372 and SE location of the front, coincided with sea level over the 75th percentile a few days earlier.
373 A similar relation was observed, but with less strength, when the position along the central line
374 was considered. However, no relationship was observed between salinity at PT and the front
375 position along the S coast. Again, this could be expected as this location is the farthest away
376 from PT. Linear and rank correlations are presented in Table 3.

Table 3: *Pearson (Spearman) correlations between SE-NW distance of the turbidity front relative to its mode and 7-day averaged sea level at Montevideo Bay with a temporal lag of 4 days (central column); and between SE-NW distance and salinity at PT (right column). Bold values indicate p-values lower than 0.05.*

	7-d sea level (4-d lag)	Salinity PT
N coast	**0.30**(**0.29**)	**-0.44**(**-0.60**)
Center	**0.40**(**0.39**)	**-0.34**(**-0.50**)
S coast	**0.25**(**0.26**)	**-0.16**(**-0.32**)

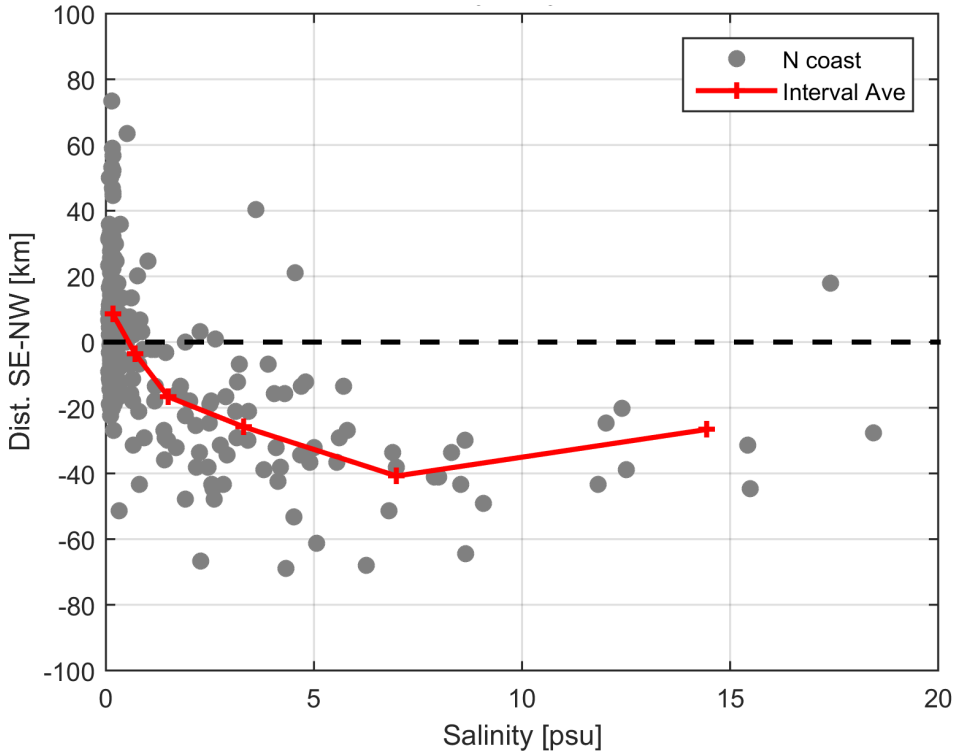

Figure 9: *Distance of the turbidity front (in km, relative to its mode) in the SE-NW direction along the N coast of the estuary versus salinity at PT (in psu, averaged +/-1 hour of the satellite's acquisition date). Interval averages are included to indicate the general trend.*

377 3.2 Numerical model

378 In this Section we present results of a novel evaluation of a numerical model previously im-
379 plemented for the Río de la Plata (Santoro, 2017). We did this by comparing turbidity and

salinity fronts obtained from the model with remote sensing results presented in Section 3.1, and in-situ information. This allowed us to identify new strengths and limitations of the model. Furthermore, using the model results, we were able to interpret remote sensing and in-situ data, contributing to advance in the understanding of the estuary dynamics.

3.2.1 Overall location

From Figure 10 it can be observed that the most frequent position of the model turbidity front was similar to the one obtained from satellite images, matching Barra del Indio geometrical feature. Both the model and satellite images showed that during 2015 the front reached far SE locations up to the Atlantic Ocean boundary, as well as NW locations into the intermediate zone. However, turbidity fronts obtained from MODIS (Figure 10(a)) showed higher dispersion and variability than the ones obtained from the model, especially along the northern coast of the estuary. These remained closer to their most frequent position (Figure 10(b-c)).

Another difference between the model and satellite results was observed close to Sanborombón Bay, where the front was positioned usually further away from the coast in the original model results (Figure 10(b)), indicating that the Bay itself had relatively high suspended sediment concentrations, which did not agree with the observations from satellite images. The new parameterization of the settling velocity (Figure 10(c)) improved results at this Bay, and also corrected some unrealistic cases in the intermediate zone of Río de la Plata. However, it failed to improve the dispersion of the front along the N coast. The salinity front (Figure 10(d)), on the other hand, showed a relatively large dispersion in its position along the center of the estuary.

3.2.2 Temporal evolution

Figure 11 shows the location of turbidity fronts obtained from MODIS and from the model, together with the location of the salinity front from the model, river discharge anomalies, and the in-situ salinity at GS during 2015. It can be seen that salinity at GS had a larger variability and reached higher values than the salinity at PT (Figure 4).

From Figure 11 it was observed that the model performed better during low discharge periods, for example, between February to July of 2015. However, the model had difficulties to capture the turbidity front location during average and high river discharge periods, for example, at the beginning of September, and during December 2015.

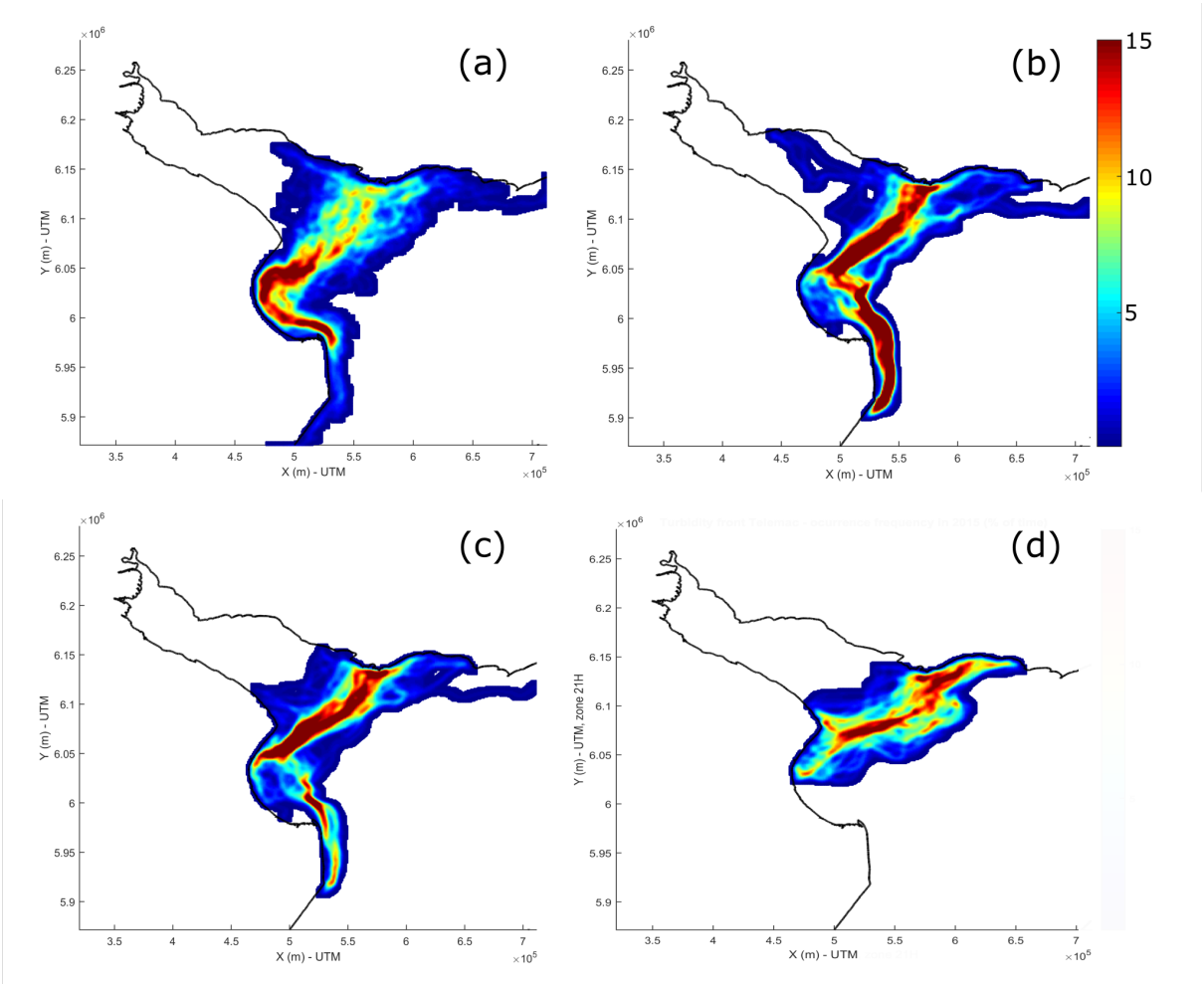

Figure 10: *Location of the turbidity front during 2015 according to: MODIS-Aqua images (a), SSC in the original numerical model (b), and SSC in the model with the new settling velocity parameterization (c). Additionally, the salinity front in the model is shown (d). The colors represent the percent of images at which the front was detected at a given place. Only matching times are considered for comparison.*

3.2.3 Relation to river discharge and in-situ salinity

Figure 12 shows the SE-NW distances obtained from satellite images and from the model against total daily river discharge for the year 2015; while the relationship with the salinity measured at GS is presented in Figure 13. Corresponding correlations are shown in Table 4.

Firstly, it should be noted that the model salinity front accurately captured the relation between the front location and river discharge. As the latter increases, the salinity front was found further to the outer zone of the Río de la Plata. The model turbidity front, on the other hand, presented a weaker relationship with the discharge (Figure 12), which did not give statistically significant correlations according to coefficients in Table 4. As it can be observed in this table (fourth row, columns three and four), the new parameterization in the model slightly

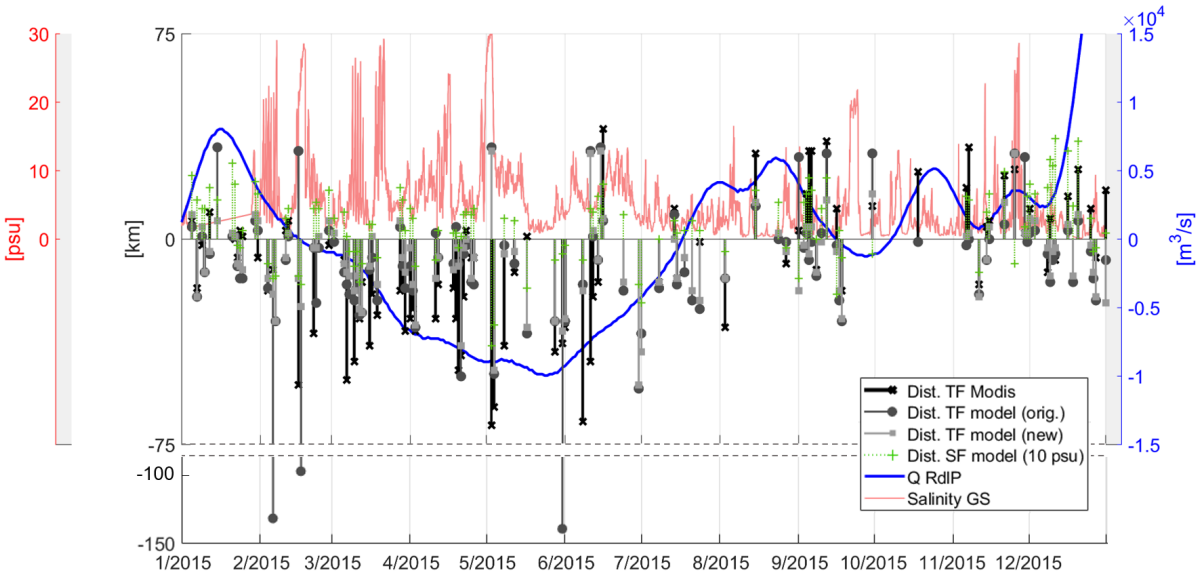

Figure 11: *Time series of turbidity and salinity front (TF and SF respectively) distances (in km) along the N coast in the SE-NW direction. Both satellite and model results are relative to the mode of the satellite's front. Discharge (Q) anomalies (in m^3/s) and salinity (in psu) at GS are also included.*

improved results for the S coast, which had negative correlation with discharge in the original version.

Secondly, according to Figure 13 and Table 4 (sixth row, second and last columns), the model salinity front showed a relation with in-situ salinity at GS along the N coast that is very similar to the relation between MODIS turbidity front and salinity at GS. As expected, these correlations decreased towards the S coast as it is further away from the field station. However, they decayed faster for model results than for satellite results. This is probably because the model was calibrated using more information located in the N coast. The relationship between the model turbidity front and in-situ salinity was much weaker. For the new settling velocity parameterization, it was observed in Figure 13 that the turbidity front distance decreased with salinity up to around 3 psu and then it remained relatively constant, while for the original model the distance initially decreased and then it increased. On the other hand, distances obtained from MODIS had a stronger relationship with lower salinity values (<3 psu) than model results, and for greater values they remained fairly constant.

3.2.4 Comparison of satellite and model results

Figure 14 and Table 5 allow for the quantitative comparison of model and satellite results. For the N coast and center lines, Figure 14 shows that the model tended to underestimate

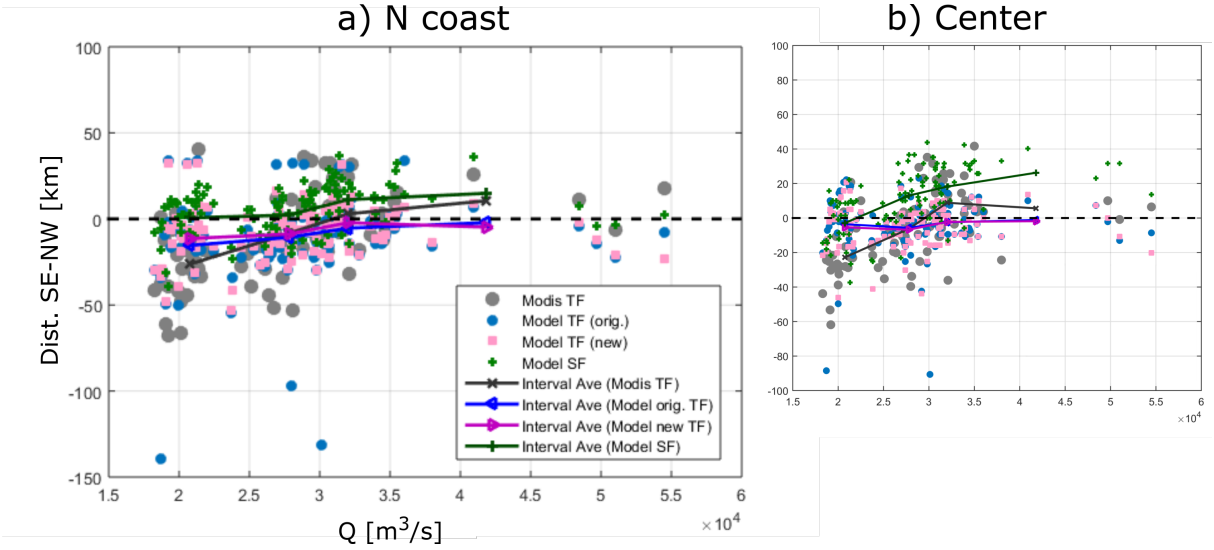

Figure 12: *Distance of turbidity and salinity fronts (TF and SF respectively, in km) along the N coast (a) and the center of the estuary (b) versus Río de la Plata discharge (Q, in m^3/s). Interval averages are included to indicate the general trend.*

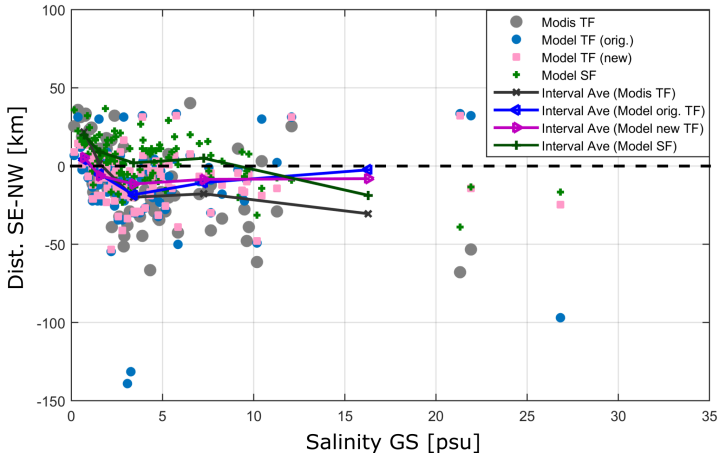

Figure 13: *SE-NW distance of the turbidity and salinity fronts (TF and SF respectively, in km) along the N coast versus salinity at GS (in psu). Interval averages are included to indicate the general trend.*

the magnitude of both positive and negative distances, but it was able to capture the trend. Additionally, the model salinity front showed relatively high correlation coefficients with MODIS turbidity front (Table 5). The S coast was where the model performed worst, but its salinity front presented positive correlation to the turbidity front from MODIS images.

Finally, Figure 15 shows some selected cases of satellite and model sediment plumes, as well as the model salinity field. They qualitatively illustrate the performance of the model in a way that cannot be captured by the previous analyses. Rows of Figure 15 are sorted chronologically: January 24th (a), March 16th (b), May 4th (c), September 12th and 17th (d-e), November 7th (f), and December 25th (g) of 2015. These dates are selected in order to compare different

Table 4: *Pearson (Spearman) correlations between SE-NW distance of the turbidity or salinity front (TF or SF respectively) with total river discharge (Q) and with in-situ salinity at GS (Salin. GS), for the year 2015. Bold values indicate p-values lower than 0.05.*

Q	MODIS TF	Model TF (orig.)	Model TF (new)	Model SF
N coast	**0.52 (0.60)**	0.14 (**0.21**)	0.12 (**0.20**)	**0.24 (0.30)**
Center	**0.53 (0.65)**	0.02 (-0.02)	0.03 (0.03)	**0.49 (0.51)**
S coast	**0.46 (0.48)**	**-0.24 (-0.20)**	0.01 (-0.03)	**0.52 (0.60)**
Salin. GS				
N coast	**-0.49 (-0.57)**	-0.04 (-0.16)	-0.05 (**-0.25**)	**-0.47 (-0.41)**
Center	**-0.49 (-0.54)**	0.00 (-0.04)	-0.02 (-0.09)	**-0.27 (-0.41)**
S coast	**-0.25 (-0.34)**	-0.05 (-0.01)	-0.05 (-0.1)	-0.05 (**-0.36**)

conditions: total discharge in the 10th (Figure 15(c)) and 90th (Figure 15(g)) percentiles; strong and persistent wind from the S-W quadrant (two-day averaged magnitude larger than 8 m/s, Figure 15 (d)); relatively strong and persistent winds from the N-E (Figure 15(a)) and S-E (Figure 15(b)) quadrants (two-day averaged magnitude larger than 6 m/s); finally, Figures 15(e-f), although they show different patterns, both occurred with mean total discharge and a few days after the occurrence of positive peaks in sea level. For both cases, instantaneous local winds -and in the previous hours- were weak, however, they presented some differences regarding the rate of change of sea level and the Uruguay river discharge. The latter (Figure 15(f)) occurred during a clear and persistent decrease of sea level, as well as positive anomaly of the Uruguay river flow; while for the case of Figure 15(e), sea level changes are negligible and the Uruguay river discharge is low.

It can be observed the large variability of the turbidity front location and patterns. In most cases, the model turbidity front location was similar to the remotely sensed one (Figure 15(f) was the exception); and the new settling velocity parameterization produced results that were slightly better than the ones obtained with the original parameterization. Most significantly, the new parameterization improved the shape and patterns of sediment plumes, for example, in Figures 15(c) and 15(e). Finally, it must be highlighted that in several cases the salinity front presented a pattern very similar to the remotely sensed turbidity front, for instance, in Figures 15(e-g).

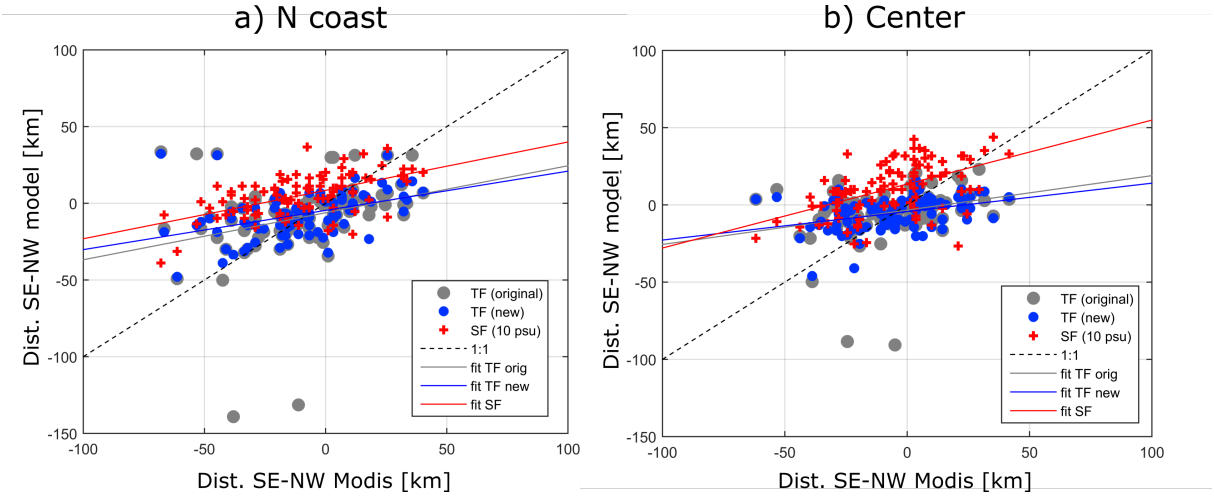

Figure 14: *Comparison of results (SE-NW distance, in km) obtained from satellite images and from numerical modeling, along the N coast (a) and the center of the estuary (b). In both panels turbidity front (TF) distances from MODIS are compared to TFs computed using the original and new parameterization in the model, and also to its salinity front (SF). Linear fits are included, as well as the 1:1 line.*

Table 5: *Pearson (Spearman) correlations between turbidity front's distances obtained from Modis images and turbidity or salinity front's (TF or SF respectively) distances obtained from the model results, for the year 2015. Bold values indicate p-values lower than 0.05.*

	Model TF (orig.)	Model TF (new)	Model SF
N coast	**0.29 (0.45)**	**0.42 (0.50)**	**0.55 (0.51)**
Center	**0.27 (0.34)**	**0.36 (0.38)**	**0.51 (0.51)**
S coast	-0.08 (-0.04)	0.08 (0.06)	**0.32 (0.35)**

4 Discussion

4.1 General location of the turbidity front

In agreement with the previous work by Framiñan & Brown (1996), the most frequent position of the turbidity front obtained from the analysis of MODIS images (Figure 3) matched approximately the location of Barra del Indio, where an important change in bathymetry occurs (Figure 1).

Regarding the role of bathymetry on the average front location, three mechanisms are considered: dilution of advected sediments from zones of lower to higher water depths; a decrease in current velocities as the estuary widens and deepens, which would increase the settling capacity of fine sediments (Simionato & Moreira, 2018; Moreira & Simionato, 2019); and larger bottom shear stress in shallower zones due to the combined effect of waves and tidal currents, which facilitates the resuspension of fine sediments (Fossati, 2013; Moreira & Simionato, 2019).

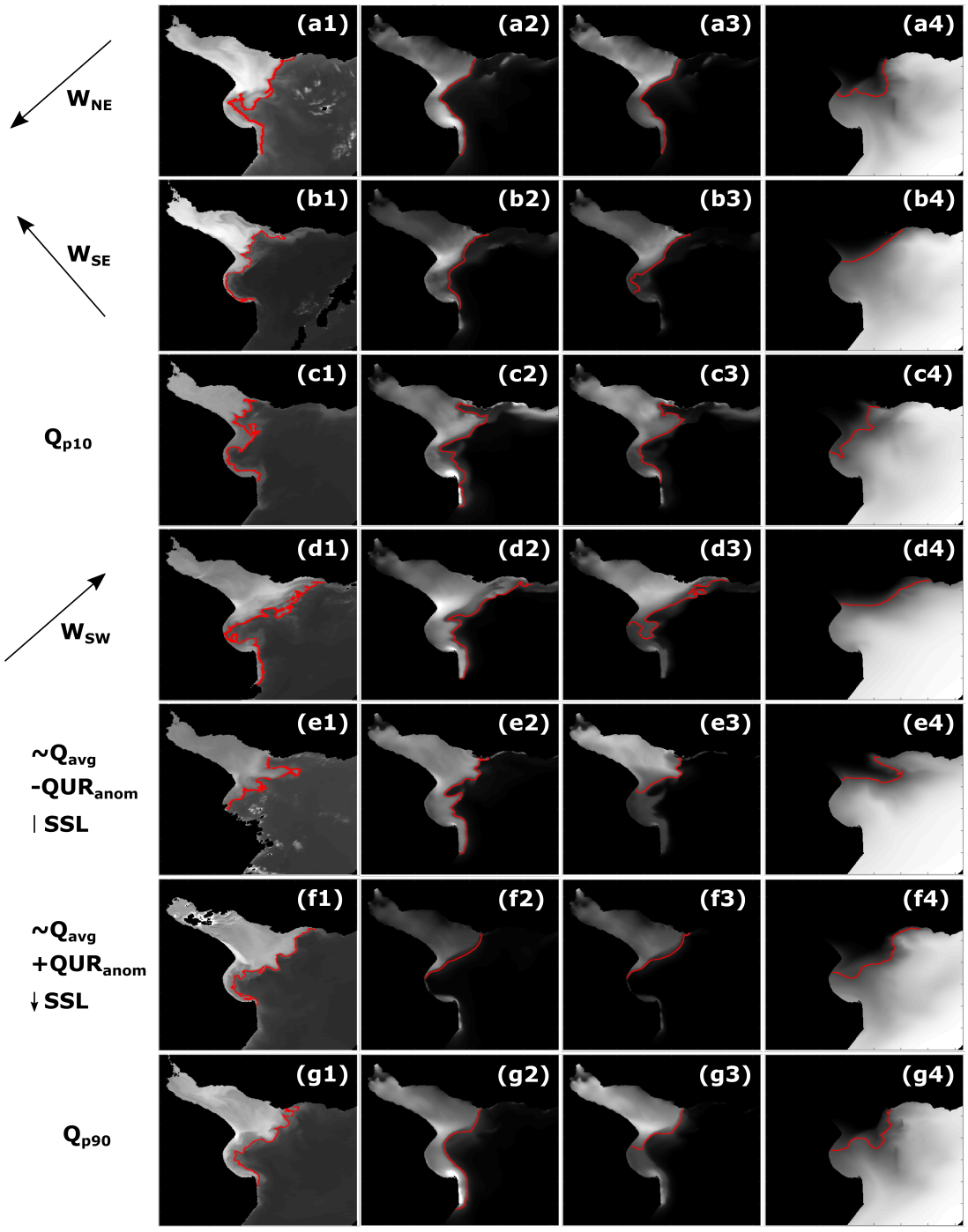

Figure 15: *Examples of turbidity fronts obtained from MODIS (a1-g1) for specific dates and forcing conditions (see text), compared to sediment plumes from the model with original settling velocity equations (a2-g2), with the new parameterization (a3-g3), and the model salinity field (a4-g4). Each row have matching dates and hours within the model temporal resolution. Panels (a2-g2) and (a3-g3) are in the same scale: from 0 (black) to 150 mg/L (white) SSC; while salinity in panels (a4-g4) scale from 0 (black) to 35 (white) psu. MODIS plumes (a1-g1) are scaled in terms of TOA reflectance (not to scale in terms of turbidity between different dates).*

The works of Fossati (2013) and Moreira & Simionato (2019) studied the global fine sediment dynamics in the Río de la Plata using numerical models with several sediment classes (fine sand, silt and clay). In the former, the interaction of suspended and bottom sediments through cycles

of erosion-advection-settling was highlighted; and when only the tributaries input of suspended sediments was considered, they remained in the inner zone of the estuary. Additionally, the recent work of Moreira & Simionato (2019) highlights the role of tides, suggesting that they determine the suspended sediment distribution pattern, while winds and waves contribute in increasing concentrations, especially in the transition and outer zones, where the effect of waves becomes particularly important in lifting suspended sediments to surface layers. Although the model in this study has one sediment class, with settling velocity corresponding to the less finer silt considered in these previous works, it succeeded in representing well the most frequent location of the turbidity front (Figure 10(b-c)). Furthermore, in several occasions the model captured very well the shape complexities of the front (Figure 15(c-d)).

Considering these previous observations, it is inferred that the most frequent location of the surface turbidity front is largely explained by the bottom shear stress and composition of bottom material. In Figure 16 the average pattern of the bottom shear stress obtained form model results for the year 2015 is shown. It is strongly influenced by bathymetry and waves in the transition to the outer zone, with some contribution from tidal currents. In addition, bottom material zones of fine (cohesive) and sandy sediments are included in the figure. It can be observed that bottom shear stresses are larger in the transition zone, and considerably decrease as depth increases rapidly seawards in the outer zone, except around the sand banks.

On the other hand, the front location distribution (Figure 3) showed an important variability along the northern coast, while in the southern coast it often followed the isobath along Sanborombón Bay, which also agrees with findings by Framiñan & Brown (1996). Bottom topography is more complex in the northern coast of the estuary (Figure 1), and Framiñan & Brown (1996) suggested that the greater depth of navigation channels along the N coast allowed a higher degree of mobility, while shallow areas constrained the movement of the front. Complementing this hypothesis, it is observed from Figure 16 that closer to the southern coast of the estuary there is a clear area of maximum bottom shear stress. This area, near Punta Piedras, is identified as an erosion zone by tides and waves (Fossati, 2013), with larger contribution of tides to the south of Punta Piedras (Moreira & Simionato, 2019), maintaining the sediments in the water column, contributing to the lower variability of the front location.

Closer to the northern coast across the transition zone, the bottom shear stress is in general lower and more heterogeneous, which is consistent with a more diffuse average location of the turbidity front. Besides shear stress, composition of bottom material imposes some limitation

on the outward location of the front, considering the availability of fine sediments that can be eroded.

Although the model presents slightly more diffuse locations of the turbidity front closer to the N coast, it shows much less variability than remote sensing results, and consequently, a more defined mode. When evaluating the model performance with different settling velocity parameterizations, it was noticed that it was particularly difficult to get the sediments to remain in suspension over large distances. According to field campaigns in Río de la Plata (performed during calm climatic conditions), suspended sediments are found to be finer than bottom material and also finer near the N coast (Fossati, Santoro, et al., 2014). Some of the calibration simulations performed by Santoro (2017) using lower settling velocities (one order of magnitude or less compared to the selected value) showed a much larger variability of the turbidity front position along the center and north coast. Hence, having a single particle class model might limit the achievable representation of the suspended sediments, especially during calm periods. The proposed synoptic validation may particularly highlight this flaw of the model, as the finest sediment fractions dominate turbidity. However, they may not be particularly important for the near-bed sediment transport and the bottom evolution near Montevideo Bay, which were the main processes considered when the model was developed.

4.2 Turbidity and salinity

The vertical structure of the salinity field in the Río de la Plata has been measured and studied by several authors (R. A. Guerrero et al., 1997; Sepúlveda et al., 2004; Simionato et al., 2007; Acha et al., 2008; R. Guerrero et al., 2010; Simionato et al., 2011). The estuary presents strong vertical stratification with a quasi-permanent salt-wedge in the southern and coastal zones (R. A. Guerrero et al., 1997; Simionato et al., 2007), while more gradual salinity profiles prevail in the northern coast during fair weather (Fossati, Santoro, et al., 2014). Stratification conditions can be destroyed by onshore winds (R. A. Guerrero et al., 1997; Simionato et al., 2007).

Regarding turbidity, the intermediate zone presents vertically uniform profiles (Fossati, Cayocca, & Piedra-Cueva, 2014), while some stratification is observed towards the transition zone, becoming stronger in the outer zone due to the influence of the salinity field (Fossati, Santoro, et al., 2014). Framiñan & Brown (1996) observe a good visual correlation between areas of maximum vertical salinity gradient and areas of maximum density of the turbidity front distribution.

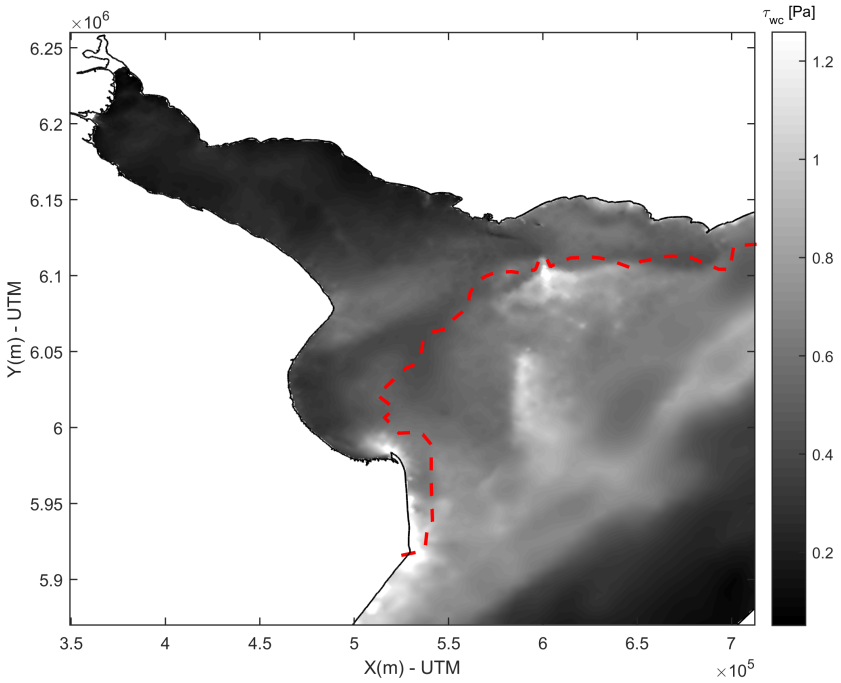

Figure 16: *Average total (currents+waves) bottom shear stress obtained from the model, matching the dates of MODIS images during 2015. The dashed line indicates the transition between fine (silt and clay) bottom material (inwards) and sand (outwards) used in the model, which is based on López Laborde & Nagy (1999).*

Considering the 3D variability of suspended sediments and the salinity field in the Río de la Plata, it is important to discuss if the fronts used in this study represent bottom or surface conditions. Remote sensing can only detect near-surface turbidity, however, the optical depth is not constant over the estuary, and in general it would increase towards the outer zone as suspended sediment concentrations decrease. The turbidity front detected in the model is also representative of near-surface conditions, and variable in depth due to the model implementation in sigma layers, being thicker in deeper (and outer least turbid) zones of the estuary. The salinity front, on the other hand, is representative of the average water column, which would be influenced by both bottom and surface salinity. It can be thought as an average salinity front, but fairly more representative of the surface considering the presence of a defined salt wedge during fair weather. According to R. A. Guerrero et al. (1997), who analyzed 29 years of salinity data in the Río de la Plata, surface salinity is controlled by the effect of winds, river discharge and the Coriolis force, presenting some seasonality, in contrast to bottom salinity that is controlled by bathymetry. In this study, we found that the model salinity front clearly responded to river discharge (Table 4).

The work of Acha et al. (2008) posed that the turbidity maximum in the Río de la Plata

559 matched the location of the salt-wedge (bottom salinity, controlled mainly by bathymetry),
560 based on results of Framiñan & Brown (1996). The presence of a salt-wedge influences estuar-
561 ine circulation, containing fresh water and sediment discharges at the area of Barra del Indio
562 (Moreira & Simionato, 2019), and it also enhances sediment flocculation. Even without con-
563 sidering the effect of enhanced flocculation by salinity, Fossati (2013) identified Barra del Indio
564 as a deposition zone. Furthermore, Dogliotti et al. (2016) observed year-long relatively high
565 turbidity values along Barra del Indio and Punta Piedras. In this work, turbidity fronts were
566 usually located seawards of the visual maximum (Figure 15), and they can be thought as the
567 boundary of near-surface influence of turbid fresh water. The detection methodology does not
568 strictly ties the front to the presence of a salt-wedge, which is not as well defined in the N
569 coast or during some wind events (R. A. Guerrero et al., 1997; Fossati, Santoro, et al., 2014).
570 In fact, in the present analysis, the turbidity front showed a good non-linear correlation with
571 both near-bottom (at PT) and near-surface (at GS) measured salinity. The good relation with
572 surface salinity is consistent with the influence of river discharge and winds in the position of
573 the turbidity front. This also explains that the location of the modeled salinity front correlated
574 well with the one detected from satellite images (Figure 14 and Table 5), showing remarkably
575 similar patterns of MODIS turbidity front and the modeled salinity front for several cases, as
576 shown in Figure 15(e-g).

577 Given on the one hand the good relationships between remotely sensed turbidity fronts
578 with in situ salinity and discharge, and on the other hand the good relationships between the
579 model salinity front with salinity time series, river discharge, and MODIS turbidity front, it was
580 concluded that the model represents well the dynamics of the salinity field at the estuarine scale,
581 particularly regarding the influence of basin discharge.

582 Furthermore, evaluating the model against remote sensing results revealed the relative im-
583 portance of salinity in the flocculation process. The incorporation of the new parameterization,
584 which directly considers the influence of salinity in the settling velocity of suspended sediments,
585 improved the general performance of the model (Table 5). More importantly, it corrected some
586 unrealistic cases and often improved spatial sediment plume patterns (Figure 15). These re-
587 sults highlight the potential contribution of using satellite images to evaluate and improve the
588 performance of numerical models.

4.3 Effect of forcings on the front location

River basin discharge, sea level (associated to meteorological tides), and local winds were evaluated as external forcing that could influence sediment dynamics through advection and resuspension processes, and hence, the location of the turbidity front.

4.3.1 River basin discharge

According to the correlation coefficients and the percentile distributions, river discharge seemed to be the main external forcing affecting the position of the surface turbidity front (Table 2 and Figure 6). This is consistent with findings in previous works (Framiñan & Brown, 1996; Nagy et al., 2008), which considered seasonal and interannual variability scales. However, it can be seen in Figure 4 that the front location can change considerably within a few days. This study adds to previous ones in: considering smaller temporal scales, which revealed a solid general trend with daily discharge; and evaluating different transects along the estuary.

Although Framiñan & Brown (1996) suggested greater importance of the Uruguay rather than the Paraná river flow, which is true when comparing them independently (Table 2), here it was found that their combined influence was greater. Furthermore, the influence of the discharge was stronger over the N coast, with low interannual variability of the correlation coefficients. It diminished considerably across the estuary towards the S coast, where correlations showed larger variability between years (Table 2). In general, rank correlations were higher, indicating that the relationship was not linear (see also Figure 5).

Results in this work are consistent with the flow corridors defined by Re & Menéndez (2006) and Piedra-Cueva & Fossati (2007). Under residual (tidal-averaged) flow in the estuary, an outflow (eastward) was observed near the Uruguayan coast, whose strength and width were fundamentally controlled by the discharge of both main tributary rivers (Piedra-Cueva & Fossati, 2007). On the contrary, in the S coast, near Sanborombón Bay, no net flow was found, which is consistent with the greater advance and discharge-dependent mobility of the turbidity front near the N coast found in this study. It is important to highlight that for neutrally-buoyant particles the residence times were greater than a month (Piedra-Cueva & Fossati, 2007), supporting the previous assertion that suspended sediments in the front region may not be directly linked to the simultaneous sediment load contributed by the tributaries.

Regarding seasonal or climatological behavior of the front location, we found that it can be inferred from the discharge of the tributaries. In terms of historic (1980-2018) seasonality,

620 the combined monthly mean discharge is higher in austral autumn-winter (April-July), and
621 presents relative minimums in September and summer months (December-February). However,
622 it should be highlighted that monthly mean discharges present a very high interannual variability.
623 Nevertheless, as a general trend, more inward locations of the turbidity front along the N
624 coast could be expected in the summer period, while eastward positions will be more often
625 achieved during autumn and winter. This agrees with the seasonal analyses made by Framiñan
626 & Brown (1996). On the other hand, in terms of interannual variability, the Río de la Plata
627 basin discharges present robust periodicities between 3 and 7 years linked to El Niño Southern
628 Oscillation (ENSO) phenomena (Mechoso & Perez-Iribarren, 1992; Robertson & Mechoso, 1998;
629 Garcia & Mechoso, 2005; Maciel et al., 2013). They are in phase and correlate well with the
630 index Niño 3.4 (Maciel et al., 2013), meaning that El Niño (La Niña) events are associated -on
631 average- with higher (lower) discharges (Nagy et al., 2008). The year 2015-2016 was classified as
632 a very strong El Niño year (NOAA, `http://www.esrl.noaa.gov/`), among the eight stronger
633 events since 1950; while 2014-2015 was a weak El Niño year, and 2016-2017 was a weak La Niña
634 year. Consistently, large discharge anomalies were observed from December 2015 to June 2016,
635 and the turbidity front was mainly found to the SE of its mode, and seawards from Montevideo
636 Bay along the N coast (Figure 4). This result reinforces the analysis of Nagy et al. (2008), who
637 studied the front position during a couple of ENSO events.

638 **4.3.2 Sea level**

639 Sea level, associated to ocean tides, was found to be a secondary forcing affecting the location
640 of the turbidity front. Astronomical tides in the Río de la Plata are dominated by the M2
641 component, and its effect could not be evaluated using daily satellite images. Nevertheless,
642 the meteorological component of the tides explain between 50-80% of the variance of sea level
643 time series in the estuary, being higher in the N coast (Santoro et al., 2013). Winds in the S
644 region of the Argentinian platform play an important role in the generation of tide waves that
645 enter the Río de la Plata: SW winds generate maximum levels, while minimums are associated
646 with W-NW winds; local winds can amplify their effect (Santoro et al., 2013). Therefore, the
647 seven-day averaged sea level time series used in this work mainly represented longer (persistent)
648 meteorological events of remote origin, with some possible amplification by local winds.

649 It was observed that salinity peaks at PT often occurred after a negative peak of the sea
650 level series, and matching a period of rising level. As salinity at PT and the turbidity front

location are well correlated, a lag of a few days was considered to compute correlations between the front distance and the averaged sea level. They were statistically significant, and the highest was obtained for a window of seven days with a lag of four days. Correlation coefficients reached values of 0.3 and 0.4 for the N coast and center, being lower for the S coast (Table 3).

To better understand the effect of this forcing, an event occurred at the beginning of May 2015 was selected (Figure 4) for its analysis with the model results. As the sea level began to rise after the occurrence of the minimum peak, currents tended to be predominantly in the inward direction. The opposite was observed after a positive peak, when the level decreased, currents were predominantly in the outward direction. This was more clearly seen along the center of the estuary, which is consistent with the higher correlations obtained between the sea level and the location of the turbidity front (Table 3). Along the coasts, lower depths and higher bottom friction may reduce this effect, as well as the more complex geometry and greater influence of the flow corridor in the N coast. In fact, along the N coast a bimodal distribution of the front location was observed after the occurrence of maximum level peaks (Figure 8), with locations near Montevideo Bay being predominant when river discharge was low, as it tended to shift the front inwards. Although currents seemed to be influenced by the time derivative of sea level, correlations between the latter and the front location were lower, suggesting that not only the changes in sea level matter, but also the preceding negative or positive level peaks.

The correlation was highest for a seven-day running average probably because longer tide wave events generated more persistent currents, which have higher chance of influencing the front position regardless of other forcings. This is consistent with findings of Simionato et al. (2006), that currents developed an equilibrium (barotropic) response with winds for processes that last more than 4 days.

4.3.3 Local winds

Regarding local winds, it was found that they need to have a relatively persistent (two-day) component in a given direction to significantly affect the location of the turbidity front. Two-day averaged wind magnitudes lower than the 75th percentile (in any direction) did not appear to strongly influence the position of the turbidity front, however, relatively strong events (average magnitude between 5 and 10 m/s) can have distinct effects. Winds from the S-W quadrant, usually known as “Pamperos”, clearly shifted the turbidity front towards the outer zone of the Río de la Plata along the N coast (Figure 7(c) and Figure 15(d)), suggesting that these winds

favored discharges along this coast. This effect was slightly weaker along the center of the estuary, and it was not observed in the S coast. Although S-W winds are not the most frequent ones, they reach the highest magnitudes. Similarly, a seaward discharge plume in both bottom and surface layers along the N zone of the Río de la Plata was found by Fossati, Santoro, et al. (2014) when studying the dynamics of the salinity field for two-day storms from the W-SW in 2010. SW winds forced a significant positive sea surface level anomaly in the intermediate estuary (Meccia et al., 2009; Santoro et al., 2013) and seaward residual flow in the entire water column near the N coast Fossati, Santoro, et al. (2014), explaining the considerable outward shift of the turbidity front.

The effect from S-E winds, called "Sudestadas", was not clearly observable from the satellite images in this work. It is possible that the available images (after discarding the ones affected by clouds) were more representative of calmer conditions regarding wind magnitude, as strong winds are associated with stormy, and cloudy, conditions. According to Nagy et al. (2008), onshore (SE) winds produce an inward shift of the front (3-day average wind magnitudes larger than 8,5 m/s); in this study, winds from the S-E quadrant did not exceed magnitudes of 7 m/s (2-day averaged), however, the example shown in Figure 15(b) (wind magnitude >6 m/s), agrees with the result of this previous work. They are also consistent with salinity field dynamics during SE storms (>10 m/s) studied by Fossati, Santoro, et al. (2014), which showed a saltwater entry from the ocean mainly near the N coast, and inward (outward) residual flow through surface (bottom) layers.

On the other hand, winds with relatively strong N components generated an inward shift near the N coast, where the front reached further inward locations, especially for N-E winds. Interestingly, when winds came form the N-E quadrant, a pronounced seaward shift of the turbidity front occurred along the center and S coast. This suggests a general circulation pattern generated by N-E winds, with an entrance along the N coast and discharge closer to the S coast. Meccia et al. (2009) noted that N winds generate negative sea level anomalies, with NE winds affecting mainly the intermediate estuary (near Montevideo), and NW the upper zone. Additionally, they noted that NE winds are usually originated after "Sudestadas", while NW winds often precede "Pamperos". These previous observations support the more marked effect on the front position caused by winds from the N-E quadrant compared to the N-W ones (Figure 7(a-b))

5 Summary and conclusions

Diverse methodologies have been used in other turbid coastal regions to study river plumes and front dynamics from satellite information, with authors using either retrieved suspended particulate matter (SPM) (Doxaran et al., 2009; Petus et al., 2014; Hu et al., 2016; Zheng et al., 2015; Abascal-Zorrilla et al., 2020), turbidity (Braga et al., 2017) or directly water leaving reflectance (Fernández-Nóvoa et al., 2017, 2019). These approaches require a proper atmospheric correction of the images, and the calibration or validation of the SPM algorithms. In this work, a novel image-based algorithm was successfully implemented to remotely detect the turbidity front in the Río de la Plata estuary, based on the histogram of the images. The turbidity level associated to the front was variable among dates, as it best represented the transition between different water masses. The approach selected here allowed evaluating the performance of a previously implemented hydro-sedimentological numerical model of the Río de la Plata in terms of spatio-temporal front dynamics. Moreover, the effect of forcing on the turbidity front location and its relation to the salinity field was studied combining the satellite observations with in-situ data and the model simulation results.

It was found that bottom shear stress (related to bathymetry, currents, and waves), together with bottom material composition, strongly influences the most frequent position and average distribution of the turbidity front. Although the importance of bottom topography was posed by Framiñan & Brown (1996), the link with shear stress and bottom material was pointed out in this work, combining satellite observations with modeling results. Previous analyses (Fossati, 2013; Moreira & Simionato, 2019) support this hypothesis, as suspended sediments in the front zone seem to be mainly related to erosion and lifting of bottom material in this area.

Furthermore, turbidity front dynamics seemed to be related to both bottom and surface salinity. The quasi-permanent salt-wedge in the Río de la Plata (R. A. Guerrero et al., 1997) is probably a better indicator of the turbidity maximum (Acha et al., 2008), which was not studied here, while the detected surface turbidity front was influenced by the same forcing as surface salinity (i.e. discharge, winds). The distance between the turbidity maximum and the detected front, together with the intensity of the former, could possibly give an estimation of the water column saline stratification, although this would need to be studied and validated with in-situ profiles in a future work.

The turbidity front location was more variable near the N coast, where bathymetry is more

744 complex and saline stratification is weaker compared to the S coast (Fossati, Santoro, et al.,
745 2014). There, the influence of river discharge and local winds was stronger. The former was
746 identified as the main external forcing, revealing a solid general pattern of behavior: when
747 discharge was high (low) the front tended to be located in the outer (intermediate) zone of the
748 estuary. Although the influence of discharge was highlighted by Framiñan & Brown (1996) in
749 seasonal and interannual time scales, here significant correlations were obtained using daily data.
750 Correlation coefficients were larger in the N coast, with relatively low inter-annual variability.
751 Furthermore, it was found that the relationship between discharge and the front position was
752 not linear, and the combined influence of both main tributaries (Paraná and Uruguay rivers)
753 was greater than their independent effect. This result is consistent with flow corridors identified
754 in the estuary (Re & Menéndez, 2006; Piedra-Cueva & Fossati, 2007).

755 Local winds needed to have a relatively persistent (two-day) component in a given direction to
756 affect the location of the turbidity front. Winds from the S-W quadrant considerably shifted the
757 turbidity front towards the outer zone along the N coast and center; while N wind components
758 tended to generate an inward shift near the N coast, as well as a seaward shift closer to the
759 S coast when they came from the N-E quadrant. However, as mentioned before, strong wind
760 events may not be adequately represented in remotely sensed information, and for example S-E
761 winds could not be evaluated. Regarding the effect of winds, this work complements the previous
762 work of Nagy et al. (2008), by analyzing different regions across the Río de la Plata and relating
763 it to salinity field dynamics based on the work of Fossati, Santoro, et al. (2014).

764 Averaged sea level, mainly associated to meteorological tides, was identified as a secondary
765 forcing, presenting higher correlations along the center of the estuary than near both coasts.
766 There, the front tended to be located seawards (inwards) a few days after the occurrence of
767 high (low) sea level peaks. The influence of persistent currents generated mainly by sea level
768 gradients of longer tide waves was identified as the probable main cause of this behavior. Along
769 the N coast the front reached inward locations more often when a few days after the occurrence
770 of low level anomalies; while a bimodal distribution was observed after high level peaks, being
771 closer to Montevideo Bay when simultaneous low discharge occurred.

772 Besides being a relevant input for the discussion and interpretation of estuarine dynamics, the
773 numerical model performance was also evaluated, finding the following strengths: it reproduced
774 very well the main location of the turbidity front, and its variability along the N coast was slightly
775 greater; the shape complexities of the front were well captured in several occasions; the salinity

field responded to the discharge and showed a strong link to remotely sensed turbidity fronts, considering correlation coefficients and shape similarities. Model results improved when the influence of salinity on sediment settling velocities was incorporated, confirming the importance of salinity in the flocculation process, and suggesting the need of considering it in future modeling efforts. On the other hand, some limitations were also found: model results do not reproduce correctly the variability of the turbidity front spatial distribution, and its relationship to river discharge. This could probably be improved by adding additional (finer) sediment classes in a future work. It is important to highlight that the model have been developed for the study of the near-bed sediment transport and bottom evolution near Montevideo Bay, nevertheless, it performed satisfactorily for the whole estuary. Future modeling efforts at our Institute will start to incorporate remote sensing data in the calibration and validation processes, as it provides spatial information that is not available from point time series. The described methodology could be readily applied to other estuaries, gulfs and seas around the globe.

6 Acknowledgments

The authors would like to thank the Agencia Nacional de Investigación e Innovació, Uruguay (ANII) for its support trough the Sistema Nacional de Investigadores (SNI) and the María Viñas Found. Fernanda Maciel was partially supported by a fellowship from the Universidad de la República. The authors would also like to thank the different organizations that made the data used in this work available: salinity data at GS for 2015 were provided by Gas Sayago S.A., Uruguay; salinity data at PT were provided by the Administración Nacional de Usinas y Transmisiones Eléctricas, Uruguay (UTE); sea level data at Montevideo Bay were provided by the Administración Nacional de Puertos, Uruguay (ANP); Paraná and Uruguay river discharges were provided by Instituto Nacional del Agua, Argentina (INA). Finally, the authors are grateful to the anonymous reviewers for their time and effort in providing insightful guidance that helped improving the work.

References

Abascal-Zorrilla, N., Vantrepotte, V., Huybrechts, N., Ngoc, D. D., Anthony, E. J., & Gardel, A. (2020). Dynamics of the estuarine turbidity maximum zone from Landsat-8 data: The case of the Maroni river estuary, French Guiana. *Remose Sensing*, *12*, 2173.

Acha, E. M., Mianzan, H., Guerrero, R., Carreto, J., Giberto, D., Montoya, N., & Carignan, M. (2008). An overview of physical and ecological processes in the Rio de la Plata estuary. *Continental Shelf Research*, *28*, 1579–1588.

Ackerman, S., Strabala, K., Menzel, P., Frey, R., Moeller, C., Gumley, L., ... Zhang, H. (2006). *Discriminating clear-sky from cloud with MODIS: Algorithm theoretical basis document.* (MOD35). University of Wisconsin - Madison; NOAA; NASA. (Version 5.0)

Alonso, R., Solai, S., & Teixeira, L. (2015). Wave energy resource assessment in uruguay. *Energy*, *93*, 683-696.

Benson, T., Villaret, C., Kelly, D., & Baugh, J. (2014). Improvements in 3d sediment transport modelling with application to water quality issues. In *23rd TELEMAC-MASCARET User Conference.* Grenoble, France.

Berasategui, A. D., Acha, E. M., & Fernández Araoz, N. C. (2004). Spatial patterns of ichthyoplankton assemblages in the Río de la Plata estuary (Argentina-Uruguay). *Estuarine, Coastal and Shelf Science*, *60*(4), 599-610.

Braga, F., Zaggia, L., Bellafiore, D., Bresciani, M., Giardino, C., Lorenzetti, G., ... Brando, V. E. (2017). Mapping turbidity patterns in the Po river prodelta using multi-temporal Landsat 8 imagery. *Estuarine, Coastal and Shelf Science*, *198*, 555-567.

Burone, L., Venturini, N., Sprechmann, P., Valente, P., & Muniz, P. (2006). Foraminiferal responses to polluted sediments in the Montevideo coastal zone, Uruguay. *Marine Pollution Bulletin*, *52*, 61-73.

Castro, J., & Reckendorf, F. (1995). *Effects of sediment on the aquatic environment: Potential NRCS actions to improve aquatic habitat* (Working Paper No. 6). Oregon State University, Department of Geosciences: Natural Resources Conservation Service.

Dee, D. P., Uppala, S. M., Simmons, A. J., Berrisford, P., Poli, P., Kobayashi, S., & more. (2011). The ERA-Interim reanalysis: configuration and performance of the data assimilation system. *Q. J. R. Meteorol. Soc.*, *137*, 553-597.

Di Polito, C., Ciancia, E., Coviello, I., Doxaran, D., Lacava, T., Pergola, N., ... Tramutoli, V. (2016). On the potential of robust satellite techniques approach for SPM monitoring in

coastal waters: implementation and application over the Basilicata Ionian coastal waters using MODIS-Aqua. *Remote Sensing*, *8*, 922.

Dogliotti, A. I., Ruddick, K., & Guerrero, R. (2016). Seasonal and inter-annual turbidity variability in the Río de la Plata from 15 years of MODIS: El Niño dilution effect. *Estuarine, Coastal and Shelf Science*, *182*, 27-39.

Dogliotti, A. I., Ruddick, K. G., Nechad, B., Doxaran, D., & Knaeps, E. (2015). A single algorithm to retrieve turbidity from remotely-sensed data in all coastal and estuarine waters. *Remote Sensing of the Environment*, *156*, 157-168.

Doxaran, D., Froidefond, J. M., Castaing, P., & Babin, M. (2009). Dynamics of the turbidity maximum zone in a macrotidal estuary (the Gironde, France): Observations from field and MODIS satellite data. *Estuarine, Coastal and Shelf Science*, *81*(3), 321-332. doi: https://doi.org/10.1016/j.ecss.2008.11.013

EDF - LNHE. (2020). *open telemac-mascaret.* Retrieved 23-3-2020, from `http://opentelemac.org`

Fernández-Nóvoa, D., Costoya, X., deCastro, M., & Gómez-Gesteira, M. (2019). Dynamic characterization of the main Cantabrian river plumes by means of MODIS. *Continental Shelf Research*, *183*, 14-27.

Fernández-Nóvoa, D., deCastro, M., Des, M., Costoya, X., Mendes, R., & Gómez-Gesteira, M. (2017). Characterization of Iberian turbid plumes by means of synoptic patterns obtained through MODIS imagery. *Journal of Sea Research*, *126*, 12-25.

Fossati, M. (2013). *Dinámica global de sedimentos finos en el Río de la Plata* (Ph.D. Thesis). Facultad de Ingeniería, Universidad de la República.

Fossati, M., Cayocca, F., & Piedra-Cueva, I. (2014). Fine sediment dynamics in the Río de la Plata. *Advances in Geosciences*, *39*, 75-80.

Fossati, M., Santoro, P., Mosquera, R., Martínez, C., Ghiardo, F., Pablo Ezzatti, F., ... Piedra-Cueva, I. (2014). Dinámica de flujo, del campo salino y de los sedimentos finos en el Río de la Plata. *RIBAGUA-Revista Iberoamericana del Agua*, *1*, 48-63.

Framiñan, M. B., & Brown, O. B. (1996). Study of the Rio de la Plata turbidity front, Part I: spatial and temporal distribution. *Continental Shelf Research*, *16*(10), 1259–1282.

862 Garcia, N. O., & Mechoso, C. R. (2005). Variability in the discharge of South American rivers
863 and in climate. *Hydrological Science*, *50*(3), 459-478.

864 Gobbelaar, J. U. (1985). Phytoplankton productivity in turbid waters. *Journal of Plankton*
865 *Research*, *7*, 653-663.

866 Gohin, F. (2011). Annual cycles of chlorophyll-a, non-algal suspended particulate matter, and
867 turbidity observed from space and in-situ in coastal waters. *Ocean Science*, *7*, 705–732.

868 Gourgue, O., Baeyens, W., Chen, M. S., de Brauwere, A., de Brye, B., Deleersnijder, E., ...
869 Legat, V. (2013). A depth-averaged two-dimensional sediment transport model for environ-
870 mental studies in the Scheldt Estuary and tidal river network. *Journal of Marine Systems*,
871 *128*, 27-39.

872 Guerrero, R., Piola, A., Molinari, G., Osiroff, A., & Jáuregui, S. (2010). *Climatología de*
873 *temperatura y salinidad en el Río de La Plata y su Frente Marítimo.* (Tech. Rep.). Instituto
874 Nacional de Investigación y Desarrollo Pesquero INIDEP, Mar del Plata. (95 p.)

875 Guerrero, R. A., Acha, E. M., Framiñan, M. B., & Lasta, C. A. (1997). Physical oceanography
876 of the Rio de la Plata estuary, Argentina. *Continental Shelf Research*, *7*, 727-742.

877 Hervouet, J.-M. (2007). *Hydrodynamics of Free Surface Flows.* Chichester, UK: John Wiley &
878 Sons, Ltd. Retrieved 2015-08-19, from `http://doi.wiley.com/10.1002/9780470319628`

879 Hu, Z., Pan, D., He, X., & Bai, Y. (2016). Diurnal variability of turbidity fronts observed
880 by geostationary satellite ocean color remote sensing. *Remote Sensing*, *8*(147), 36-68. doi:
881 doi:10.3390/rs8020147

882 López Laborde, J., & Nagy, G. (1999). *Hydrography and sediment transport characteristics of*
883 *the Río de la Plata: a review.* Springer.

884 Maciel, F., Díaz, A., & Terra, R. (2013). Multi-annual variability of streamflow in La Plata
885 Basin. part i: observations and links to global climate. *International Journal of River Basin*
886 *Management*, *11*(4), 345-360.

887 Martínez, C., Silva, J., Dufrechou, E., Santoro, P., Fossati, M., Ezzatti, P., & Piedra-Cueva, I.
888 (2015). Towards a 3d hydrodynamics numerical modeling system for long term simulations of
889 the río de la plata. In *36th iahr world congress.*

Meccia, V. L., Simionato, C. G., Fiore, M. E., D'Onofrio, E. E., & Dragani, W. C. (2009). Sea surface height variability in the Río de la Plata estuary from synoptic to inter-annual scales: Results of numerical simulations. *Estuarine, Coastal and Shelf Science*, *85*, 327–343.

Mechoso, C. R., & Perez-Iribarren, G. (1992). Streamflow in southeastern South America and the Southern Oscillation. *Journal of Climate*, *5*, 1535-1539.

Mehta, A. J. (2014). *An introduction to hydraulics of fine sediment transport* (Vol. 38). World Scientific.

Moreira, D., & Simionato, C. G. (2019). Modeling the suspended sediment transport in a very wide, shallow, and microtidal estuary, the Río de la Plata, Argentina. *Journal in Advances of Modeling Earth Systems.*, *11*, 3284–3304.

Moreira, D., Simionato, C. G., Dragani, W., Cayocca, F., & Tejedor, M. L. C. (2016). Characterization of bottom sediments in the Río de la Plata estuary. *Journal of Coastal Research*, *32*(6), 1473–1494.

Moreira, D., Simionato, C. G., Gohin, F., Cayocca, F., & Tejedor, M. L. C. (2013). Suspended matter mean distribution and seasonal cycle in the Río de la Plata estuary and the adjacent shelf from ocean color satellite (MODIS) and *in-situ* observations. *Continental Shelf Research*, *68*, 51-66.

Nagy, G. J., Severov, D. N., Pshennikov, V. A., De los Santos, M., Lagomarsino, J. J., Sans, K., & Morozov, E. G. (2008). Rio de la Plata estuarine system: Relationship between river flow and frontal variability. *Advances in Space Research*, *41*, 1876–1881.

Otsu, N. (1979). A threshold selection method from gray-level histograms. *IEEE Trans. Systems, Man, and Cybernetics*, *9*(1), 62–66.

Petus, C., Marieu, V., Novoa, S., Chust, G., Bruneau, N., & Froidefond, J.-M. (2014). Monitoring spatio-temporal variability of the Adour River turbid plume (Bay of Biscay, France) with MODIS 250-m imagery. *Continental Shelf Research*, *74*, 35-49.

Piedra-Cueva, I., & Fossati, M. (2007). Residual currents and corridor of flow in the Río de la Plata. *Applied Mathematical Modelling*, *31*, 564-577.

Piola, A. R., Romero, S. I., & Zajaczkovski, U. (2008). Space-time variability of the Plata plume inferred from ocean color. *Continental Shelf Research*, *28*, 1556-1567.

Re, M., & Menéndez, A. N. (2006). Desarrollo de capas de mezcla entre los corredores de flujo del Río de la Plata interior. *XXII Congreso Latinoamericano de Hidráulica*. (Ciudad Guyana, Venezuela, October 2006)

Robertson, A. W., & Mechoso, C. R. (1998). Interannual and decadal cycles in river flows of southeastern South America. *Journal of Climate*, *11*(10), 2570-2581.

Santoro, P. (2017). *Modelación numérica de la hidrodinámica y dinámica de sedimentos finos en la Bahía de Montevideo* (Ph.D. Thesis). Facultad de Ingeniería, Universidad de la República.

Santoro, P., Fossati, M., & Piedra-Cueva, I. (2013). Study of the meteorological tide in the río de la plata. *Continental Shelf Research*, *60*, 51–63. Retrieved 2015-12-02, from `http://linkinghub.elsevier.com/retrieve/pii/S0278434313001180` doi: 10.1016/j.csr.2013.04.018

Santoro, P., Fossati, M., Tassi, P., Pham Van Bang, D., Huybrechts, N., & Piedra-Cueva, I. (2016). 2d and 3d numerical study of the montevideo bay hydrodynamics and fine sediment dynamics. In *23rd TELEMAC-MASCARET User Conference.* Paris, France.

Sepúlveda, H. H., Valle-Levinson, A., & Framiñan, M. B. (2004). Observations of subtidal and tidal flow in the Río de la Plata estuary. *Cont. Shelf Res.*, *24*, 509-525.

Simionato, C. G., Meccia, V. L., Dragani, W. C., Guerrero, R., & Nuñez, M. (2006). Río de la Plata estuary response to wind variability in synoptic to intraseasonal scales: Barotropic response. *Journal of Geophysical Research*, *111*, C09031.

Simionato, C. G., Meccia, V. L., Guerrero, R., Dragani, W. C., & Nuñez, M. (2007). Río de la Plata estuary response to wind variability in synoptic to intraseasonal scales: 2. currents' vertical structure and its implications for the salt wedge structure. *Journal of Geophysical Research*, *112*, C07005.

Simionato, C. G., & Moreira, D. (2018). Modeling the processes that control fine sediments transport in the Río de la Plata estuary. *Journal of Coastal Research.*, *85*, 31–35.

Simionato, C. G., Moreira, D., Re, M., & Fossati, M. (2011). *Estudio de la dinámica hidro-sedimentológica del Río de la Plata: Observación y modelación numérica de los sedimentos finos.* (Tech. Rep.) Proyecto FREPLATA RLA 99/G31.

947 Underwood, G. J. C., & Kromkamp, J. C. (1999). Phytoplankton productivity in turbid waters.
948 *Advances in Ecological Research*, *29*, 93-153.

949 van Leussen, W. (1999). The variability of settling velocities of suspended fine-grained sediment
950 in the ems estuary. *Journal of Sea Research*, *41*, 109–118.

951 Xia, X. M., Li, Y., Yang, H., Wu, C. Y., Sing, T. H., & Pong, H. K. (2004). Observations on
952 the size and settling velocity distributions of suspended sediment in the pearl river estuary,
953 china. *Continental Shelf Research*, *24*, 1809–1826.

954 Zhan, W., Wu, J., Wei, X., Tang, S., & Zhan, H. (2019). Spatio-temporal variation of the
955 suspended sediment concentration in the Pearl River Estuary observed by MODIS during
956 2003-2015. *Continental Shelf Research*, *172*, 22-32.

957 Zheng, G., DiGiacomo, P., Kaushal, S., Yuen-Murphy, M.A., & Duan, S. (2015). Evolution of
958 sediment plumes in the Chesapeake Bay and implications of climate variability. *Environ. Sci.*
959 *Technol.*, *49*, 6494–6503. doi: https://doi.org/10.1021/es506361p